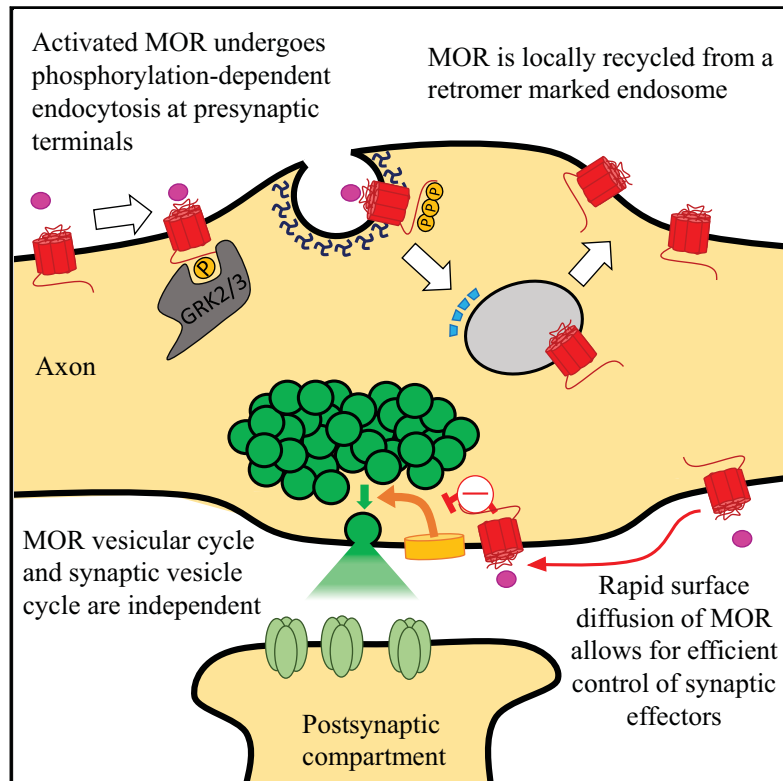


Neuron

A Discrete Presynaptic Vesicle Cycle for Neuromodulator Receptors

Graphical Abstract



Authors

Damien Jullié, Miriam Stoeber, Jean-Baptiste Sibarita, ..., Terrence J. Sejnowski, Eric Hosy, Mark von Zastrow

Correspondence

mark@vzlab.org

In Brief

Presynaptic inhibition is presently thought to require clustering of neuromodulator receptors at the surface of terminals. Jullié et al. show that opioid receptors are diffusely distributed and delineate an alternate strategy using receptor mobility and local endocytic cycling.

Highlights

- d Opioid receptors are diffusely distributed and laterally mobile on the axon surface
- d Opioid receptors are phosphorylated and internalized at presynaptic terminals
- d Opioid receptors locally recycle separately from the synaptic vesicle cycle
- d Lateral mobility and allostery suggest a new strategy for presynaptic neuromodulation

A Discrete Presynaptic Vesicle Cycle for Neuromodulator Receptors

Damien Jullié,^{1,2} Miriam Stoeber,^{1,2,3} Jean-Baptiste Sibarita,^{4,5} Hanna L. Zieger,^{4,5} Thomas M. Bartol,⁶ Seksiri Arttamangkul,⁷ Terrence J. Sejnowski,⁶ Eric Hosy,^{4,5} and Mark von Zastrow^{1,2,8,*}

¹Department of Cellular and Molecular Pharmacology, University of California, San Francisco School of Medicine, San Francisco, CA 94158, USA

²Department of Psychiatry, University of California, San Francisco School of Medicine, San Francisco, CA 94158, USA

³Department of Cell Physiology and Metabolism, University of Geneva, 1211 Geneva, Switzerland

⁴Interdisciplinary Institute for Neuroscience, UMR 5297, Centre National de la Recherche Scientifique, 33077 Bordeaux, France

⁵Interdisciplinary Institute for Neuroscience, University of Bordeaux, 33077 Bordeaux, France

⁶Howard Hughes Medical Institute, Salk Institute for Biological Studies, La Jolla, CA 92037, USA

⁷The Vollum Institute, Oregon Health and Science University, Portland, OR 97239, USA

⁸Lead Contact

*Correspondence: mark@vzlab.org

<https://doi.org/10.1016/j.neuron.2019.11.016>

SUMMARY

A major function of GPCRs is to inhibit presynaptic neurotransmitter release, requiring ligand-activated receptors to couple locally to effectors at terminals. The current understanding of how this is achieved is through receptor immobilization on the terminal surface. Here, we show that opioid peptide receptors, GPCRs that mediate highly sensitive presynaptic inhibition, are instead dynamic in axons. Opioid receptors diffuse rapidly throughout the axon surface and internalize after ligand-induced activation specifically at presynaptic terminals. We delineate a parallel regulated endocytic cycle for GPCRs operating at the presynapse, separately from the synaptic vesicle cycle, which clears activated receptors from the surface of terminals and locally reinserts them to maintain the diffusible surface pool. We propose an alternate strategy for achieving local control of presynaptic effectors that, opposite to using receptor immobilization and enforced proximity, is based on lateral mobility of receptors and leverages the inherent allostery of GPCR-effector coupling.

INTRODUCTION

Appropriate information processing in neural circuits critically relies on modulation of synaptic neurotransmission by G protein-coupled receptors (GPCRs). A widespread mechanism by which GPCRs regulate synaptic function is G protein-linked inhibition of synaptic vesicle exocytosis at terminals (Brown and Sihra, 2008). Presynaptic inhibition can occur in the absence of a diffusible second messenger intermediate by local coupling of receptors to G protein-linked effector proteins, such as voltage-gated calcium channels associated with individual

active zones (Herlitze et al., 1996; Wilding et al., 1995). Such spatially delimited signaling by GPCRs poses a fundamental cell biological challenge because synapses are typically small in size relative to axon length and sparsely distributed (Pfenninger, 2009).

Another interesting aspect of presynaptic inhibition is its potentially high sensitivity. Some peptide neuromodulators, for example, inhibit presynaptic release at low nanomolar concentrations (Pennock and Hentges, 2011; Werling et al., 1987) that correspond to only a few ligand molecules, on average, within the volume of a typical presynaptic terminal. Moreover, a number of GPCRs can maintain highly sensitive inhibition of transmitter release under conditions of prolonged or repeated ligand exposure that characteristically desensitize postsynaptic GPCR signaling processes (Pennock et al., 2012; Wetherington and Lambert, 2002). The ability of GPCR signaling at terminals to achieve and maintain high ligand sensitivity is remarkable, pointing to a need to better understand the cell biology of GPCRs in axons.

The present understanding is derived largely from the study of family C GPCRs, particularly metabotropic γ -aminobutyric acid type B (GABA-B) receptors and metabotropic glutamate (mGlu) receptors. These GPCRs cluster on terminals by binding to presynaptic scaffold proteins or pre-coupling to effectors at active zones, solving the problem of spatially delimited signaling through enforced proximity (Boudin et al., 2000; Corti et al., 2002; Dalezios et al., 2002; Laviv et al., 2011; Shigemoto et al., 1996; Somogyi et al., 2003; Vargas et al., 2008; Vigot et al., 2006). GABA-B receptors resist internalization in axons although they internalize in the somatodendritic membrane (Vargas et al., 2008), and internalization of mGlu receptors causes sustained loss of presynaptic signaling (Pelkey et al., 2008). Together, these observations support a paradigm in which GPCR function at the presynapse requires receptors to be immobilized at the terminal surface and not to internalize after activation.

It remains unknown whether this is the only cellular strategy for achieving local control, particularly when one considers family A GPCRs—such as opioid peptide receptors, D2 dopamine

receptors, and CB1 cannabinoid receptors—that produce strong presynaptic inhibition but are not obviously clustered on the presynaptic surface. Rather, these GPCRs localize both on the presynaptic surface and along the axon shaft domain clearly outside of synapses, and some of these GPCRs are also found at internal membranes in axons (Dudok et al., 2015; Mengual and Pickel, 2002; Ny ri et al., 2005; Sesack et al., 1994; Svingos et al., 1997; Wang et al., 1996). Nevertheless, family A GPCRs comprise the largest class of signaling receptors overall and the largest group of neuromodulator receptors operating at the presynapse.

Opioid peptide receptors provide a clear example. The mu-type opioid receptor (MOR) is a family A GPCR that mediates both presynaptic inhibition and postsynaptic neuromodulatory effects of endogenous opioid peptides and is a primary target of clinically important opioid analgesic drugs (Corder et al., 2018; Darcq and Kieffer, 2018; Kieffer and Evans, 2009). MORs localize on terminals but also along the axon shaft (Svingos et al., 1997), but presynaptic inhibition mediated by MORs achieves high sensitivity (Pennock and Hentges, 2011) and remains sensitive under conditions of prolonged or repeated ligand exposure, whereas postsynaptic MOR responses rapidly desensitize (Fyfe et al., 2010; Lowe and Bailey, 2015; Pennock and Hentges, 2011; Pennock et al., 2012). The mechanism underlying postsynaptic MOR desensitization is reasonably well understood based on a conserved GPCR regulatory template (Gainetdinov et al., 2004; Williams et al., 2013) initiated by ligand-induced phosphorylation of the MOR cytoplasmic tail by GPCR kinases (GRKs) followed by receptor internalization (Alvarez et al., 2002; Arttamangkul et al., 2018; Just et al., 2013; Yousuf et al., 2015). Do opioid receptors fail to engage the conserved phosphorylation-endocytosis machinery in axons? Might opioid receptors reveal a distinct cell biology of GPCRs at the presynapse?

Here we address and answer these questions. We show that MORs do engage the conserved phosphorylation-endocytosis machinery in axons and do so specifically at terminals. However, rather than driving an overall loss of functional receptors to produce net signal desensitization, the conserved phosphorylation-endocytosis machinery is deployed differently in axons to support an alternate strategy for local effector control based on receptor diffusion rather than immobilization.

RESULTS

Surface Distribution and Ligand-Induced Internalization of MORs in Axons

We began by examining the distribution of MORs in axons of cultured medium spiny neurons (MSNs). GFP-labeled MORs (MOR-GFPs) were visualized along the entire axon length, both inside and outside of presynaptic terminals marked by synaptophysin-mCherry (syp-mCh; Figure 1A). Linear correlation analysis, achieved by determining the variation in MOR-GFP fluorescence intensity along the axon length, indicated a moderate fluorescence increase that overlapped with terminals (Figure 1B). We observed similar localization of endogenous MORs in cultured habenula neurons using a specific antibody (UMB3) validated previously by others (Lupp et al., 2011) and in our hands (Figure S1A). Endogenous MORs localized along axons

inside and outside of synapses labeled with VGLUT2 (Figure 1C). To specifically examine receptors present in the plasma membrane, we used extracellular FLAG epitope (SSF-MOR) tagging (Whistler and von Zastrow, 1998) or fusion of the GFP variant superecliptic pHluorin (SEP-MOR), whose fluorescence is quenched in acidic intracellular compartments (Sankaranarayanan et al., 2000; Yu et al., 2010). These results revealed a diffuse surface distribution of MORs, with a small (~15%) degree of enrichment at synapses (Figures S1B and S1C). Because UMB3 recognizes both recombinant and endogenous MOR, we used it to estimate the degree of recombinant receptor expression achieved in our experiments. Depending on the transfection method used, recombinant receptor expression ranged from comparable with endogenous level to less than 10-fold overexpression (Figure S1D). Surface receptor distribution was diffuse over this range, indicating that it is not an artifact of excessive expression. Application of the opioid peptide agonist DAMGO ([D-Ala², N-Me-Phe⁴, Gly⁵-o]-enkephalin, 10 μ M) caused MOR-GFPs to visibly accumulate at terminals (Figure 1D). Line scan analysis verified this accumulation through a sharpening of the fluorescence profile (Figure 1E) without a detectable change in syp-mCh distribution (Figure S1E). DAMGO-induced accumulation of MORs was also evident for endogenous receptors, as indicated by localization in bright puncta preferentially localized at synapses (Figure 1F). Epitope-tagged MORs exhibited DAMGO-induced relocalization after surface antibody labeling using two different epitopes (FLAG and hemagglutinin [HA]). In time-lapse image series, receptor-containing puncta were resolved within axons in confocal optical sections (Figure 1G) and exhibited saltatory movements (Video S1). This suggests that MORs undergo ligand-induced internalization in axons, a conclusion that was further supported by uptake of a fluorescent opioid peptide (Arttamangkul et al., 2000) by endogenous opioid receptors (Figure S1F).

We verified regulated internalization of MORs in axons using ammonium chloride (NH₄Cl) to dequench SEP-MOR fluorescence in acidic internal compartments (Sankaranarayanan et al., 2000). Under basal conditions, addition of NH₄Cl had no significant effect on SEP-MOR fluorescence distribution or intensity along axons, indicating that receptors are present almost exclusively at the axon surface (Figures 1H and 1I). Within 30 min after application of opioid peptide, NH₄Cl produced a significant fluorescence increase, indicating that ~17% of the total axonal SEP-MOR pool accumulated in an acidic intracellular compartment (Figures 1H and 1I).

MOR Endocytosis in Axons Is Phosphorylation-Dependent and Occurs at Presynaptic Terminals

Regulated endocytosis of MORs in the somatodendritic compartment is dynamin dependent and requires phosphorylation of the MOR cytoplasmic tail by GRKs (Lowe et al., 2015; Williams et al., 2013; Yousuf et al., 2015). To investigate whether MOR regulation is similar in axons, we examined the effects of experimental manipulations that inhibit specific steps of this conserved mechanism. We assessed MOR accumulation into puncta using an unbiased accumulation index (STAR Methods). The DAMGO-induced increase in the MOR accumulation index, indicating punctate redistribution of receptors (Figures 2A and

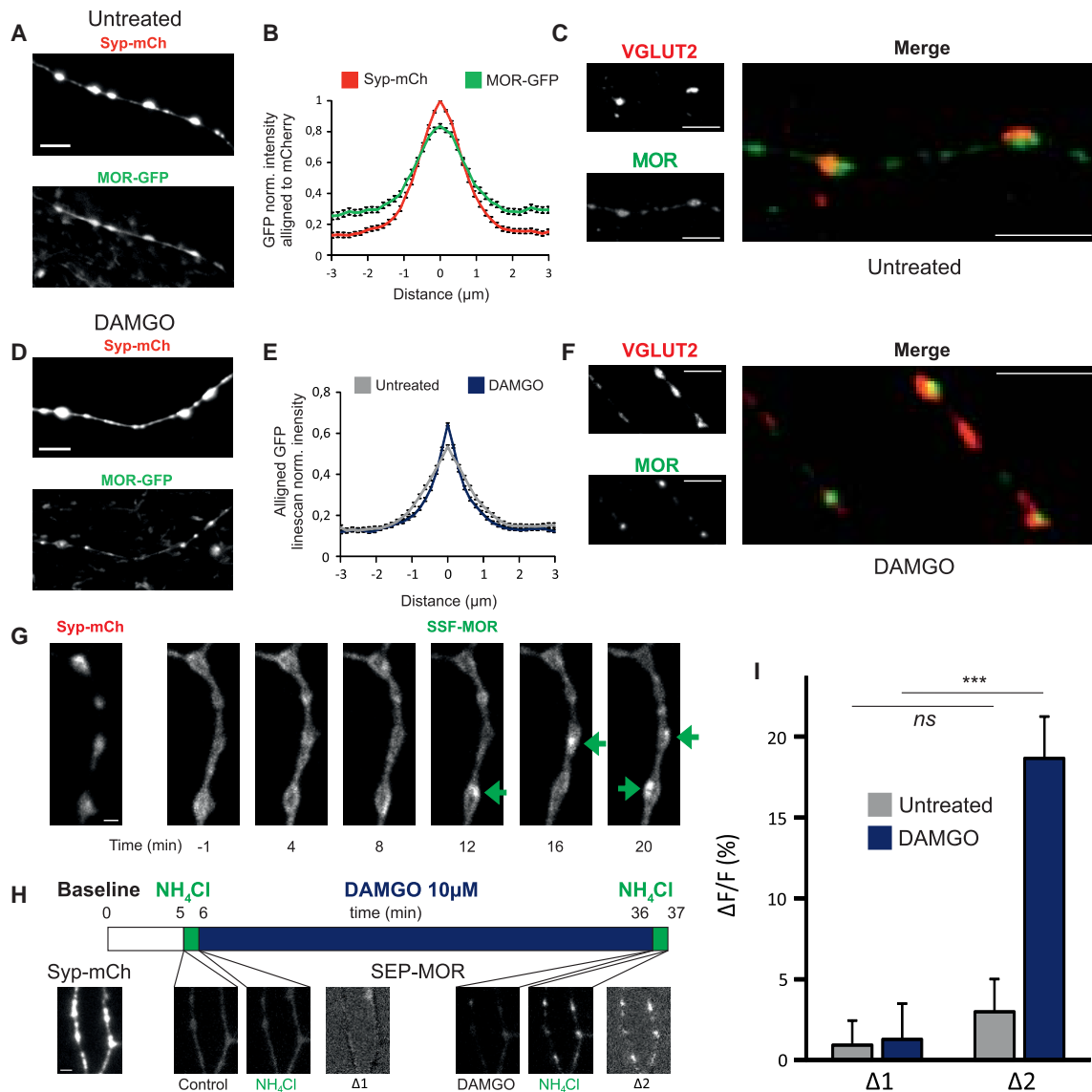


Figure 1. MORs Undergo Ligand-Dependent Endocytosis in Axons

(A) Representative oblique illumination (HiLo) images of axons of cultured MSNs expressing the synaptic marker synaptophysin-mCherry (syp-mCh) and MOR-GFPs. Scale bar, 5 μ m.

(B) Normalized MOR-GFP line scan fluorescence aligned to the maximal value along the normalized syp-mCh line scan fluorescence (n = 177 synapses from 33 cells).

(C) Maximal projection from spinning disc images of habenula neurons. Axons are labeled with VGLUT2 and show diffuse distribution of endogenous MORs. Scale bars, 5 μ m.

(D) Axons of MSNs expressing MOR-GFPs and syp-mCh 20 min after incubation with DAMGO (10 μ M). Scale bar, 5 μ m.

(E) Normalized MOR-GFP line scan fluorescence aligned to the maximal value along the line scan, untreated n = 177 synapses (same dataset as A; a different normalization method was used to highlight intensity and distribution changes), DAMGO (10 μ M, 20 min, n = 280 synapses from 39 neurons).

(F) Maximal projection of spinning disc images of axons of habenula neurons treated with DAMGO (10 μ M) for 20 min. Note the accumulation of endogenous MORs at bright puncta. Scale bars, 5 μ m.

(G) Spinning disc confocal images of cultured MSNs expressing syp-mCh and SSF-MORs, surface-labeled with Alexa 488-coupled anti-FLAG antibody (M1-a488). DAMGO (10 μ M) was added at time 0. Note the accumulation of intraluminal puncta (green arrows). Scale bar, 1 μ m.

(H) Experimental protocol and representative images of MSN axons expressing SEP-MORs and syp-mCh. After 5 min of baseline, the solution was exchanged for a solution containing 50 mM NH₄Cl. A similar exchange was performed after 30 min of perfusion with control solution or a solution containing 10 μ M DAMGO. Frames were taken before and 1 min after perfusion with 50 mM NH₄Cl; Δ represents the difference between the frame in NH₄Cl and the preceding frame. Note the increased fluorescence in the presence of ammonium chloride after 30 min of agonist. Scale bar, 5 μ m.

(I) Quantification of the normalized fluorescence difference along lines drawn on axons obtained as in (H), before (Δ 1) or after (Δ 2) 30 min of control solution (n = 6 cells) or 10 μ M DAMGO (n = 10 cells). Error bars represent SEM; ***p < 0.001.

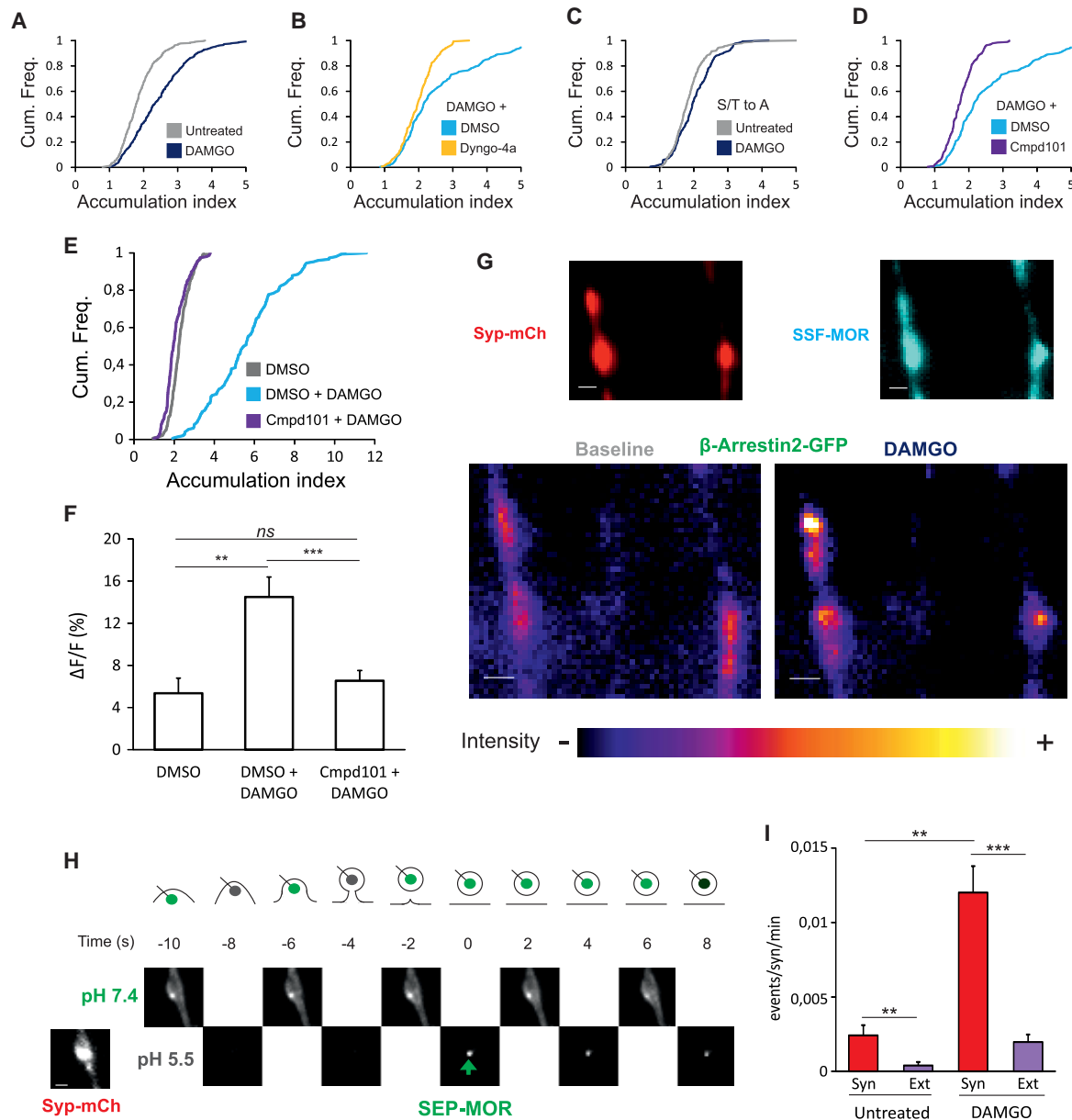


Figure 2. MOR Endocytosis Occurs at Presynaptic Terminals and Requires Receptor Phosphorylation

(A) Accumulation index plots estimating receptor redistribution by heterogeneity of the fluorescence signal of SSF-MORs (labeled with M1-a647) along MSN axons. The right shift observed in cumulative frequency curves elicited by DAMGO (10 μ M for 20 min, n = 255 axons) relative to the untreated condition reflects SSF-MOR punctate accumulation associated with internalization (n = 316 axons, p < 0.001).

(B) The same as (A), comparing MSNs treated with DAMGO (10 μ M) and Dyngo-4a (30 μ M) (n = 169 axons) with DAMGO (10 μ M) and DMSO vehicle (n = 220 axons); p < 0.001.

(C) The same as (A) for MSNs expressing syp-mCh and the phosphorylation-deficient MOR mutant (S/T to A) in untreated neurons (n = 275 axons) with neurons treated with DAMGO (10 μ M for 20 min) (n = 168 axons); p < 0.01.

(D) The same as (A), comparing MSNs treated with DAMGO (10 μ M) and Cmpd101 (30 μ M) (n = 196 axons) or cells treated with DAMGO (10 μ M) and DMSO vehicle (replotted from B); p < 0.001.

(E) The same as (A), comparing endogenous MOR in SV2-marked axons of habenula neurons treated with DMSO vehicle only (gray curve, n = 139 axons), DMSO + DAMGO (10 μ M, blue curve, n = 148 axons), or Cmpd101 (30 μ M) + DAMGO (10 μ M) (purple curve, n = 156 axons); p < 0.001 under all conditions.

(F) Normalized fluorescence difference of lines drawn on axons from MSNs expressing SEP-MORs and syp-mCh before and after NH_4Cl . Cells were treated for 20 min with DMSO vehicle (n = 17 cells), DMSO + DAMGO (10 μ M) (n = 19 cells), or Cmpd101 (30 μ M) + DAMGO (10 μ M) (n = 19 cells).

(G) Representative HiLo images of axons of MSNs expressing syp-mCh (top left panel), SSF-MORs surface labeled with M1-a647 (top right panel), and β -arrestin2-GFP before (bottom left) and after (bottom right) addition of DAMGO (10 μ M). Note the redistribution of the GFP signal at synaptic puncta. GFP images are scaled the same. Scale bars, 1 μ m.

(legend continued on next page)

S2A), was reduced in the presence of the dynamin inhibitor Dyngo-4a (Figures 2B and S2A). Mutation of phosphorylation sites in the MOR cytoplasmic tail that are required for regulated endocytosis (Just et al., 2013) inhibited DAMGO-induced MOR redistribution (Figures 2C and S2A). We further verified this using compound 101 (Cmpd101), a chemical inhibitor of GRK2/3 shown previously to block MOR endocytosis via a conserved phosphorylation-dependent mechanism (Lowe et al., 2015; Figures 2D and S2A). We also established this key result for endogenous MORs using the same accumulation assay (Figure 2E) and verified that this represents blocking of internalization of MORs in axons using the SEP-MOR dequenching assay (Figure 2F). Another clue is that β -arrestin-2-GFP redistributed in axons in response to DAMGO-induced activation of SSF-MORs, and, interestingly, the highest degree of local concentration was observed at terminals (Figure 2G). Because β -arrestins are known to operate as endocytic adaptor proteins for MORs (Whistler and von Zastrow, 1998; Zhang et al., 1998), this suggested the possibility that regulated endocytosis of MORs occurs specifically in terminals.

To directly visualize sites of MOR endocytosis, we used the pulsed pH (ppH) protocol to resolve individual MOR-containing endocytic events in living neurons based on the endocytic scission event rendering SEP-labeled receptors resistant to extracellular application of a membrane-impermeant acidic buffer (pH 5.5 MES) (Merrifield et al., 2005; Rosendale et al., 2017). We took advantage of the fact that SEP-MORs localize almost exclusively on the axon surface of neurons in the absence of opioid agonist, with little internal accumulation verified by essentially complete quenching of fluorescent signal upon perfusion of pH 5.5 buffer (Figure S2B). By alternating pH 5.5 and pH 7.4 perfusion at 0.5 Hz and using oblique illumination (HiLo) to image the entire axon with a high signal-to-noise ratio, nascent SEP-MOR-containing endocytic vesicles were resolved in DAMGO-treated cells as acid-resistant fluorescent puncta appearing abruptly in a pH 5.5 imaging frame (Figures 2H, S2C, and S2D). The frequency of these events was dramatically increased in the presence of DAMGO (Figure 2I). Remarkably, the vast majority (85% \pm 4%) of these MOR-containing endocytic events localized specifically to presynaptic terminals (Figure 2I). These results directly demonstrate that MORs undergo regulated, phosphorylation-dependent endocytosis in axons and further indicate that this regulated endocytic process occurs largely at presynaptic terminals.

MOR Internalization Defines a Discrete Population of Presynaptic Endosomes

Having localized endocytic events specifically at presynaptic terminals, we next used epitope tagging and antibody uptake

to examine the location of MORs after internalization. Surface-labeled SSF-MORs accumulated in endosomal structures that localized within terminals but were not restricted there because they were also observed in the axon shaft (Figure 3A). MOR-containing endosomes were present in 53.8% \pm 5.0% of terminals imaged along the axon ($n = 10$ neurons), and 62.3% \pm 2.3% (same dataset) of the MOR-containing endosomes imaged were located within terminals. Considering that synapses account for approximately one-third of axonal length (29% \pm 3%, same dataset) in our cultures, this represents an \sim 4-fold bias of endosome location in terminals relative to the axon shaft. When examined in time-lapse image series, MOR-containing endosomes were not static and moved bidirectionally into and out of synapses and occasionally exchanged between neighboring terminals (Figure 3B). Despite similar instantaneous speeds both inside and outside of synapses (Figure S3A), MOR-containing endosomes exhibited more confined movements inside of synapses, explaining the synaptic bias of MOR-containing endosomes by kinetic trapping in terminals (Figure S3B). Although MOR-containing endosomes were often observed within presynaptic terminals, their dynamics in axons clearly distinguish them from the synaptic vesicle pool.

To our knowledge, such a discrete presynaptic endosomal compartment has not been characterized previously, and we sought a molecular marker to identify it separately from a receptor cargo. The retromer complex was an attractive candidate because this multiprotein sorting device marks endosomes through which various signaling receptors transit in somata and dendrites (Choy et al., 2014). Further, the retromer has been localized to internal membranes in terminals but is not detected on synaptic vesicles (Takamori et al., 2006; Vazquez-Sanchez et al., 2018). To test the possibility that the retromer is a marker of MOR-containing presynaptic endosomes, we examined, in DAMGO-exposed habenula neurons, the localization of the retromer, marked by endogenous VPS35, relative to endogenous VGLUT2 and MORs. Punctate staining of VPS35 was abundant in axons and synapses marked by VGLUT2, and it overlapped with endogenous MORs (Figure 3C). Because of the small size of presynaptic terminals, we considered the possibility that this apparent colocalization was coincidental. Using structured illumination microscopy to increase spatial resolution, endogenous VPS35 puncta clearly overlapped MOR-containing endosomes and were separate from VGLUT2 (Figure 3D). GFP-labeled VPS29, a distinct but stoichiometrically assembled subunit, revealed retromer-associated endosomes in axons and synapses in live neurons. These endosomes were present irrespective of agonist application, and their density scaled with synapse density (Figure S3C). Surface-labeled SSF-MORs redistributed from the axon surface into these endosomes after

(H) Top panel: illustration of the endocytic process and the expected SEP signal during the ppH protocol (green represents fluorescence, gray represents quenching). Scission of an endocytic vesicle during the pH 7.4 step generates an acid-resistant fluorescent spot on the following pH 5.5 step. Bottom panel: cultured MSNs expressing syp-mCh and SEP-MOR imaged with HiLo during the ppH protocol. Apparition of a pH 5.5 resistant signal (green arrow) indicates an endocytic event. Scale bar, 1 μ m. The contrast is doubled for pH 5.5 frames for better visibility.

(I) Frequency of endocytic events detected with the ppH inside (red) or outside (purple) of synapses in the presence ($n = 58$ cells) or absence ($n = 23$ cells) of DAMGO (10 μ M). Frequencies were normalized to the number of synapses in the imaging field for comparison between acquisitions. Note the increased frequency in the presence of agonist and the proportion of synaptic events.

Error bars represent SEM; ** $p < 0.01$, *** $p < 0.001$.

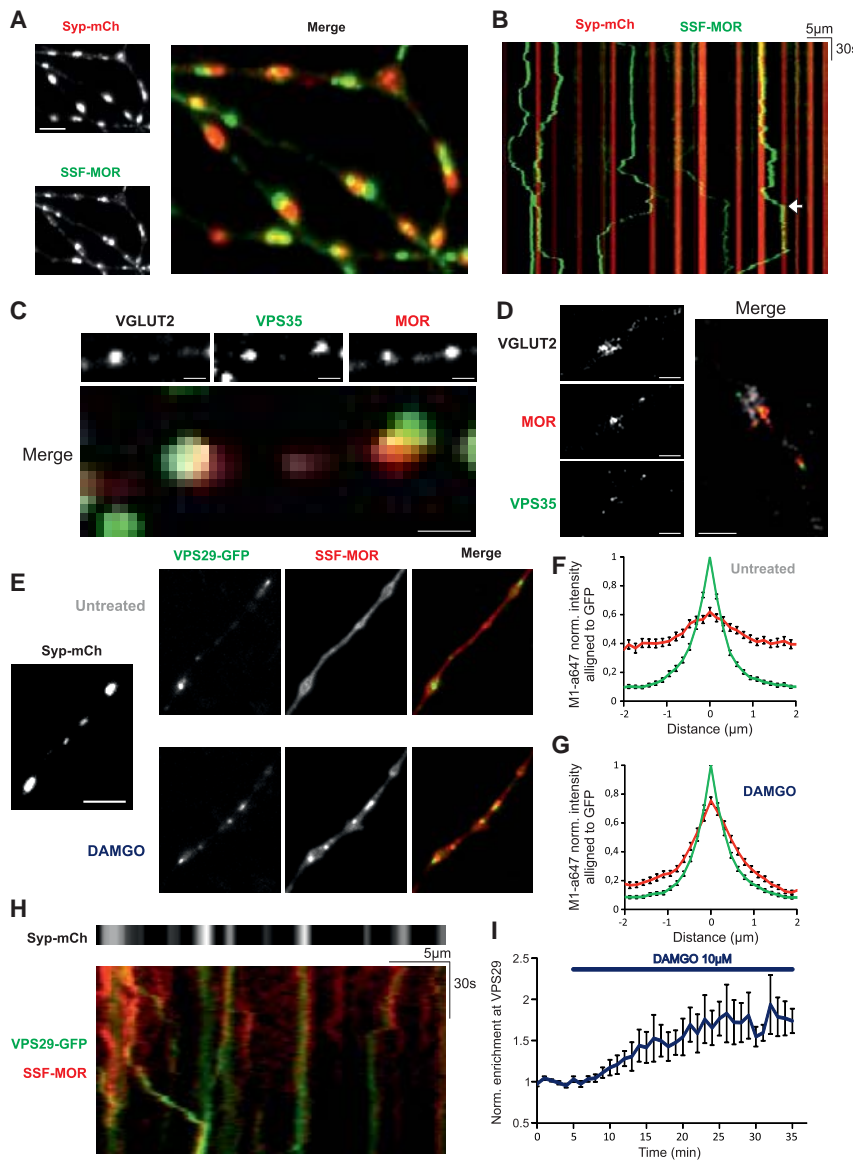


Figure 3. Endocytosed MOR Defines a Discrete Population of Presynaptic Endosomes that Are Marked by the Retromer

(A) HiLo images of cultured MSNs expressing syp-mCh and SSF-MORs, surface labeled with M1-a488 and incubated with DAMGO (10 μM for 20 min). MORs containing endosomes exhibit strong synaptic localization. Scale bar, 5 μm.

(B) Kymograph obtained with 1-Hz HiLo imaging under the same condition as in (A). Note the bidirectional, saltatory movement of individual endosomes (arrow).

(C) Single plane of spinning disc confocal images of endogenous VPS35 in axons of habenula neurons labeled with VGLUT2 and treated with DAMGO (10 μM for 20 min). Note the colocalization of endogenous MOR-containing endosomes with VPS35. Scale bars, 1 μm.

(D) Single plane of structured illumination microscopy images under the same conditions as for (C). Scale bars, 1 μm.

(E) Representative HiLo images of cultured MSNs expressing the retromer complex subunit VPS29-GFP with syp-mCh and SSF-MORs, surface-labeled with M1-a647 before (top panel) and after (bottom panel) DAMGO (10 μM) addition. SSF-MORs are diffuse in the absence of agonist and exhibit little colocalization with VPS29-GFP. After agonist addition, receptors redistribute in puncta that colocalize with VPS29-GFP. Scale bar, 5 μm.

(F) From the same experimental setup as (E), normalized M1-a647 line scan fluorescence aligned to the maximal value along the normalized VPS29-GFP fluorescence before DAMGO (10 μM) addition (from 12 cells, n = 105 endosomes).

(G) The same as (F) after DAMGO (10 μM). Note the increase in the linear correlation coefficient (from 12 cells, n = 113 endosomes).

(H) Kymograph obtained with 1-Hz HiLo imaging of VPS29-GFP (green) and surface-labeled SSF-MORs (red) 20 min after DAMGO (10 μM) addition. MORs containing endosomes and VPS29-GFP move together in axons of MSNs marked with Syp-mCh (top panel).

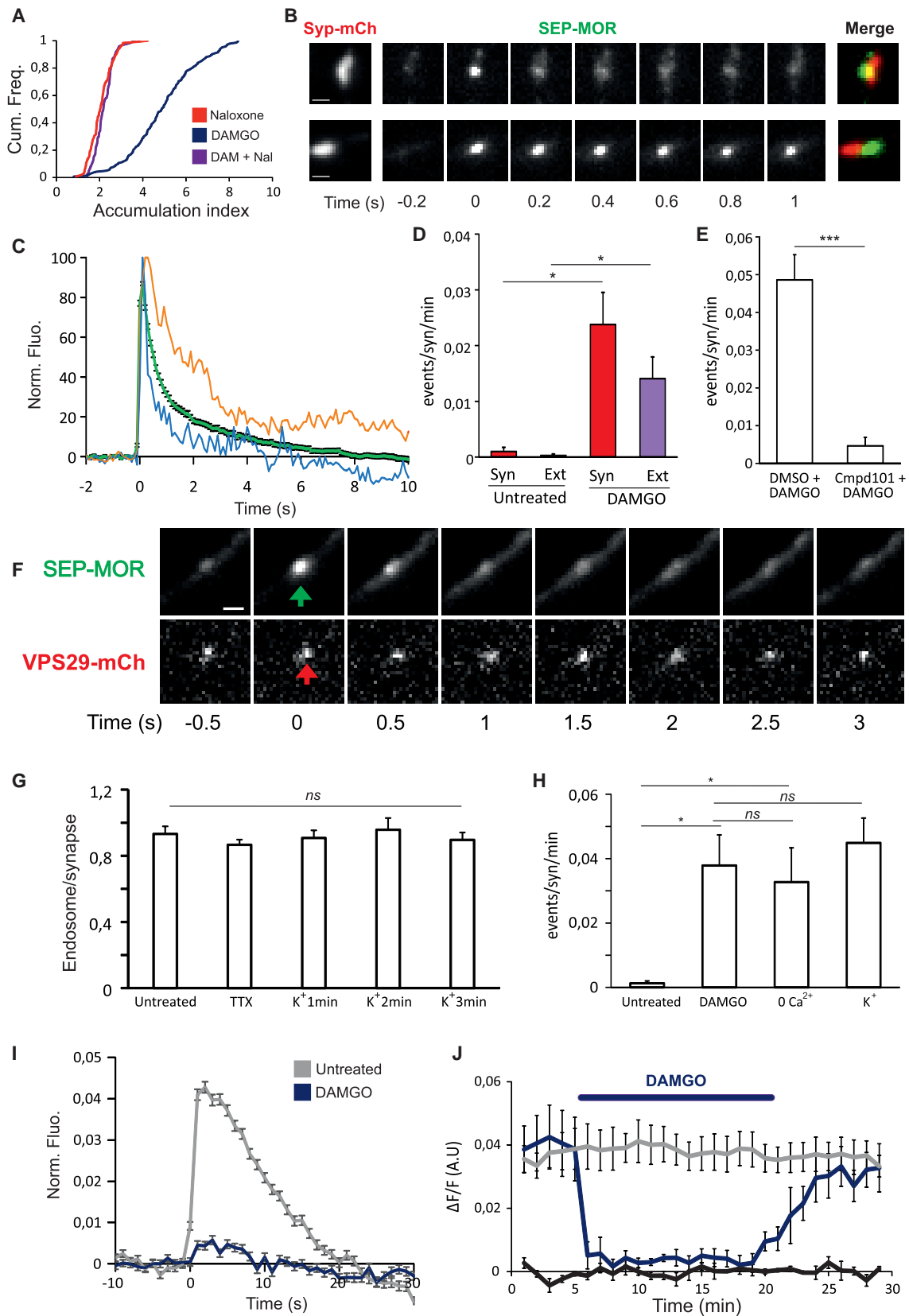
(I) Time course of the normalized fluorescence of SSF-MORs surface labeled with M1-a647 at segmented VPS29-GFP-positive endosomes (n = 12 cells, the same dataset as in F and G).

Error bars represent SEM.

application of DAMGO (Figure 3E), as confirmed by line scan analysis (Figures 3F and 3G; linear correlation coefficient of 0.62 ± 0.03 under basal conditions, n = 105 endosomes, 0.75 ± 0.02 after DAMGO addition, n = 113 endosomes from 12 cells, $p < 0.001$). Similar to the behavior observed by labeling with MORs, retromer-marked endosomes were mobile in axons and trapped at synapses, with occasional movements observed between adjacent synapses. Internalized MOR was indeed present in the same endosomes because labeled SSF-MORs and retromers moved together in axons of agonist-exposed neurons (Figure 3H; Video S2). Segmentation of the VPS29-GFP signal to follow retromer-marked endosomes in the axon revealed progressive accumulation of surface-labeled SSF-MORs in response to DAMGO application (Figure 3I). Together, these results indicate that the retromer defines a discrete population of presynaptic endosomes that accumulate internalized MORs.

A Parallel Regulated Endocytic Cycle Operating at the Presynapse

The behavior of retromer-marked endosomes that traffic MORs, particularly their local bidirectional movements, is different from previously described receptor-containing endosomes marked by TrkA, which exhibit long-range retrograde transport. Thus we asked whether the distinct endosomes containing MORs might mediate local recycling. As a first step to address this question, we investigated the reversibility of MOR accumulation in presynaptic endosomes. The punctate distribution of endogenous MORs produced in axons by DAMGO application fully reversed within 30 min after terminating MOR activation by application of the competitive MOR antagonist naloxone (Figure 4A). We next attempted to directly visualize recycling of MORs in axons. To do so, we imaged neurons expressing SEP-MORs together with a synaptic marker at 10 Hz, a speed that is



(legend on next page)

sufficient to resolve individual exocytic fusion events into the plasma membrane by dequenching (Yu et al., 2010). When neurons were imaged after 20 min in the continuous presence of DAMGO, a condition that drives MOR internalization to a steady state, exocytic events were detected at the axon surface as diffraction-limited bursts of increased fluorescence intensity (Figures 4B and 4C). For the majority of these insertion events, SEP-MOR fluorescence decayed within seconds (Figures 4C and S4A). This is consistent with fusion of the receptor-containing vesicle followed by lateral spread. A minority of insertion events had a longer lifetime before disappearing (Figure S4A), a behavior observed previously in somata and dendrites and attributed to transient fusion-fission at the insertion site (Jullié et al., 2014). To determine whether such events also occur in axons, we imaged SEP-MORs during ppH perfusion and observed that some receptor-containing exocytic insertion events observed at pH 7.4 became resistant to quenching in the following pH 5.5 frame (Figure S4B), indicating transient fusion-fission at the insertion site.

The frequency of MOR-containing surface insertion events significantly increased after incubation with an agonist both in synapses and extrasynaptic regions (Figure 4D). This suggests an endocytic origin of the insertion events. Verifying this, preincubation of neurons with Cmpd101 to block endocytosis significantly reduced the frequency of SEP-MOR insertion events (Figure 4E). We also noticed, from the analysis of individual MOR-containing insertion events, that approximately two-thirds occurred directly at terminals and one-third extrasynaptically (Figure 4D), similar to the distribution of MOR-containing endosomes in axons. This suggested that these endosomes might directly mediate local insertion. Supporting this, when

SEP-MOR insertion events were imaged relative to mCherry-tagged VPS29, SEP-MOR insertion was detected adjacent to a retromer-marked endosome (Figure 4F). Together, these results demonstrate that presynaptic MOR enters and transits a regulated endocytic cycle that is initiated specifically at presynaptic terminals, mediated by retromer-marked presynaptic endosome carriers, and completed by local vesicular re-insertion from these endosomes both in synapses and the adjacent axon shaft domain.

Endosomes distinct from synaptic vesicles are known to accumulate in presynaptic terminals under conditions of strong stimulation, but these structures are typically transient and resolve into synaptic vesicles (Kokotos and Cousin, 2015). In contrast, retromer-marked endosomes were observed in terminals under basal conditions. Further, their number was not significantly changed under all conditions tested, from strong stimulation using high potassium to blockade of electrical activity with tetrodotoxin (Figures 4G and S4C). We then asked whether manipulations of the synaptic vesicle cycle affect presynaptic MOR insertion. To do so, we preincubated neurons with DAMGO for 20 min to drive SEP-MOR internalization to a steady state and then imaged SEP-MOR insertion events. Neither depletion of extracellular calcium to block synaptic vesicle release (Figure S4D) nor high potassium to stimulate synaptic vesicle exocytosis significantly changed the frequency of SEP-MOR surface insertion events (Figure 4H). We conversely tested the effect of stimulating MOR endocytic cycling on the synaptic vesicle cycle. Using VGAT-SEP to monitor synaptic vesicle exocytosis elicited by electrical field stimulation (Santos et al., 2013), activation of MOR with DAMGO strongly inhibited synaptic vesicle exocytosis (Figure 4I). The endocytosis-defective mutant version of MOR

Figure 4. MORs Undergo a Complete Membrane Trafficking Cycle in Axons that Is Independent of the Synaptic Vesicle Cycle

- (A) Accumulation index of endogenous MORs, measured on axons of habenula neurons stained with SV2 for cells treated with naloxone (10 μ M for 30 min) (red curve, n = 124 axons), cells treated with DAMGO (100 nM for 20 min) (blue curve, n = 142 axons), or cells treated with DAMGO (100 nM for 20 min) followed by naloxone (10 μ M for 30 min) (purple curve, n = 120 axons). $p < 0.001$ for DAMGO against the two other conditions, not significant for naloxone against DAMGO + naloxone.
- (B) After 20 min of treatment with DAMGO (10 μ M), single insertion events containing SEP-MORs appear as sudden bursts of fluorescence at the membrane of cultured MSNs imaged in HiLo. Two representative examples are shown, where insertion occurs at synapses labeled with syp-mCh (top panel) or outside (bottom panel). Note the difference in fluorescence decay for both events and the apparent surface diffusion of SEP-MORs (top panel). Scale bars, 1 μ m.
- (C) Average normalized fluorescence curves of single insertion events observed after 20 min of incubation with DAMGO (10 μ M) (green curve, n = 324 events from 16 cells). Blue and orange curves represent the corresponding normalized fluorescence quantification of the events in (B) (top and bottom events, respectively).
- (D) Frequency of SEP-MOR insertion events in the presence (n = 16 cells) or absence (n = 6 cells) of agonist inside or outside of synapses. For each cell, frequencies were normalized to the number of synapses in the imaging field for comparison between acquisitions.
- (E) Frequency of SEP-MOR insertion events monitored in axons of MSNs after incubation with Cmpd101 (30 μ M) + DAMGO (10 μ M) (n = 7 cells) or vehicle (DMSO) + DAMGO (10 μ M) (n = 8 cells).
- (F) Example of an SEP-MOR insertion event (green arrow) at VPS29-mCh labeled endosomes (red arrow) imaged in MSNs with HiLo at 2 Hz after 20 min of incubation with DAMGO (10 μ M). Scale bar, 1 μ m.
- (G) Normalized density of VPS29-GFP-marked endosomes in axons of MSNs labeled with syp-mCh under untreated conditions (n = 153 axons from 42 cells), after 1 h incubation with tetrodotoxin (n = 47 axons from 20 cells), or after 1, 2 and 3 min incubation with a solution containing 50 mM KCl (n = 35 axons from 10 cells).
- (H) Normalized frequency of SEP-MOR insertion events in axons of MSNs under untreated and DAMGO conditions replotted from the sum of (D). Under the two other conditions, neurons were incubated with DAMGO (10 μ M) for 20 min and then imaged in a solution containing DAMGO (10 μ M) without calcium (0 Ca^{2+} , n = 6 cells) or containing 50 mM KCl without DAMGO (K^+ , n = 8 cells).
- (I) In axons of MSNs, the GABA transporter fused to SEP (VGAT-SEP) localizes to synaptic vesicles that undergo exocytosis upon 10-Hz electrical field stimulation. The normalized average fluorescence increase of VGAT-SEP at synapses of neurons co-expressing SSF-MORs reports synaptic vesicle exocytosis and is inhibited after perfusion of DAMGO (10 μ M) (n = 1970 individual measurements from 5 stimulations on synapses from 5 cells).
- (J) Normalized average amplitude of VGAT-SEP fluorescence increase at synapses of MSNs expressing SSF-MORs. The black curve represents the amplitude of unstimulated cells (n = 5 cells) and blue and gray curves the amplitudes of cells stimulated with 10 action potentials at 10 Hz every minute and perfused with (n = 5 cells) or without (n = 10 cells) DAMGO (10 μ M), respectively.
- Error bars represent SEM; * $p < 0.05$, *** $p < 0.001$.

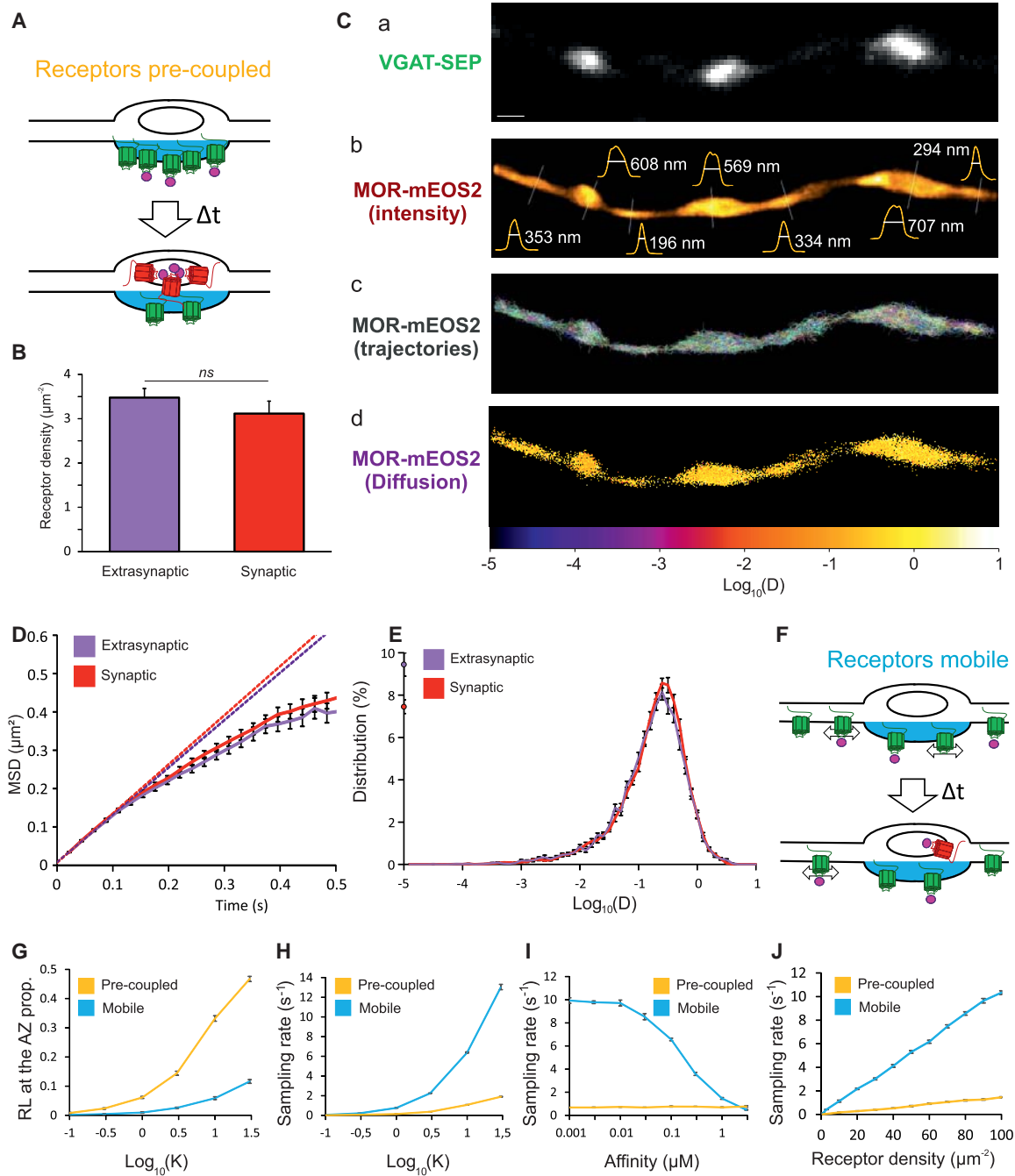


Figure 5. An Alternative Strategy for Local GPCR Control of Presynaptic Effectors Enabled by Rapid Lateral Diffusion of Receptors

(A) Schematic of a putative pre-coupled model where naive receptors (green) bind ligand and undergo activation directly at the presynapse (blue). After some time (Δt), receptors are inactivated (red) and removed from the axonal plasma membrane, which leads to a decrease in the naive receptor pool.

(B) Density of receptors in axons calculated from dSTORM images of hippocampal neurons stained for endogenous MORs and GAD67 ($n = 7$ synaptic, 17 extrasynaptic areas).

(C) HiLo image of an axonal segment of a MSN expressing VGAT-SEP as a synaptic marker (Ca) and the associated reconstructed super-resolution image from single-molecule detections of MOR-mEOS2 (Cb). Line scans across the axon show important diameter variations as quantified by the width at half maximum on the super-resolution image. Single-molecule trajectories can be reconstructed from single-molecule detections (Cc) and analyzed to extract diffusion coefficients and generate diffusion maps (Cd). Scale bar, 1 μm .

(D) Mean square displacement curves of SEP-MOR single-molecule trajectories obtained with an ATTO647-conjugated anti-GFP nanobody using uPAINT on axons of MSNs labeled with syp-mCh. Dotted lines represent linear fits on the first 4 time points associated with the two different regions and illustrate Brownian motion ($n = 46$ synaptic, 34 extrasynaptic areas from 7 cells).

(E) Distribution of diffusion coefficients obtained with uPAINT (the same dataset as in D).

(legend continued on next page)

(MOR S/T to A) similarly blocked electrically evoked synaptic vesicle exocytosis (Figure S4E). This indicates that inhibition of the synaptic vesicle cycle is a consequence of MOR signaling rather than endocytosis and that signaling by MOR from the presynaptic plasma membrane is sufficient to block the synaptic vesicle cycle. The ability of SSF-MORs to inhibit synaptic vesicle exocytosis was sustained during 15 min of agonist application, verifying, in our system, a complete lack of detectable desensitization of the presynaptic MOR response (Figure 4J). We further verified that presynaptic inhibition mediated by endogenous MOR is resistant to desensitization in habenula neurons (Figure S4F). In light of our previous findings, this shows that activation of MOR drives the receptor into its endocytic cycle while producing sustained inhibition of the synaptic vesicle cycle. Altogether, these data indicate that the MOR endocytic cycle, although it coexists at synapses with the synaptic vesicle cycle, operates separately and is regulated independently.

MORs Are Rapidly Mobile throughout the Axon Surface

Sustained MOR-mediated presynaptic inhibition is fully consistent with previous physiological observations (Fyfe et al., 2010; Lowe and Bailey, 2015; Pennock and Hentges, 2011; Pennock et al., 2012), but it raises a paradox with respect to the previously established cellular paradigm because we now recognize activation-induced internalization of MORs specifically at terminals. If MORs accumulated on the surface of boutons represent a dedicated pool of immobilized receptors, then we would expect internalization at this location to terminate responsiveness, as is the case for mGlu7 (Pelkey et al., 2008; Figure 5A). This paradox prompted us to investigate in more detail the nature of MOR accumulation at the surface of terminals.

The higher fluorescence of labeled MORs on the surface of boutons could reflect a pool of receptors clustered on the terminal surface by immobilization, as for family C GPCRs, but it could also result without such clustering from variations in axon morphology that are not possible to resolve using diffraction-limited fluorescence imaging (Chéreau et al., 2017). Clustering of receptors at terminals would result in an increased density at this location. We tested this for endogenous MORs using dSTORM (direct stochastic optical reconstruction microscopy), a form of localization microscopy that enables single-molecule detection and counting (Haas et al., 2018), applying this method to detect individual receptors in axons and determine their density (Figure S5A). The density was the same inside and outside of synapses (Figure 5B), suggesting that MORs are not clustered at the presynapse. Presynaptic boutons are larger in diameter than the axon shaft, and we reasoned that an enlarged membrane area occupied by MORs at boutons could produce apparent enrichment despite equal receptor density on the axon membrane. We tested this using PALM (photoactivation localization

microscopy), another super-resolution method that resolves individual molecules by stochastic photoconversion of MORs fused with the photoconvertible protein mEos2 (McKinney et al., 2009). The results indicate that MORs indeed explore a larger membrane area at terminals than in the axon shaft (Figures 5Ca and 5Cb). Further, to search for an immobilized receptor pool, we analyzed individual receptor trajectories from the live image series (Manley et al., 2008; Figure 5Cc). This revealed a homogeneous population of mobile receptors (Figure S5B) with an average diffusion coefficient of $0.299 \pm 0.008 \mu\text{m}^2 \text{s}^{-1}$ ($n = 33$ regions from 14 cells), consistent with a rapidly diffusing receptor pool throughout the axon (Figure S5B) and no preferential immobilization at synapses (Figures 5Cd and S5C). To specifically track surface receptors, we used uPAINT (universal point accumulation in nanoscale topography), another super-resolution method in which surface receptors are labeled in live cells at low density (Giannone et al., 2013). Analysis of SEP-MOR trajectories tracked using ATTO647-labeled anti-GFP nanobody indicated that receptors freely diffuse both inside and outside of synapses (Figure 5D), verifying rapid lateral mobility of SEP-MORs throughout the axon surface (Figure 5E), and that SEP-MOR mobility was not detectably perturbed after acute application of DAMGO (Figure S5D). Photoactivation of MOR-PAGFP in axons confirmed, at the population level, rapid lateral mobility of receptors in axons and lack of a detectable immobile fraction at synapses (Figures S5E and S5F), and this was the case both in the absence and presence of DAMGO (Figure S5F). Together, these results indicate that MOR is rapidly mobile throughout the axon surface and that accumulation at boutons in diffraction-limited images is a consequence of axon morphology.

An Alternate Cellular Strategy for Local Presynaptic Neuromodulation by GPCRs

A key difference relative to the previously established paradigm is that MOR is dynamic and mobile in axons rather than immobilized at presynaptic terminals. When one considers the organization of axons, with effectors restricted to terminals that are sparsely distributed along the axon length, the potential advantage of receptor immobilization is clear but the potential utility of lateral mobility is not. We noticed that MOR diffusion on the axon surface is sufficiently fast that receptors can move over multiple microns within the known residence time of an opioid peptide ligand (Birdsong et al., 2013). This suggests that MORs can bind ligand at a distance from the synapse and use lateral diffusion to enter the synapse while still in a ligand-bound state. The ability of GPCRs to bind ligand and couple to effectors in distinct, allosterically coupled steps is well known. We propose that lateral diffusion enables an extended version of this allostery, where ligand-receptor binding can occur at a distance from the site of receptor-effector coupling in the terminal.

(F) Schematic as in (A) of a mobile model where receptors diffuse freely in and out of synapses (arrows) and receptors can bind ligand outside of the synapse and diffuse in the active zone while in a ligand-bound state.

(G) Proportion of receptors bound to ligand at the active zone for different values of K .

(H) Frequency of independent signaling complexes (sampling efficiency) generated by the two models for different values of K .

(I) Sampling efficiency of the two models for different ligand affinity values.

(J) Sampling efficiency for receptor densities covering the reported levels of endogenous receptor expression.

Error bars represent SEM.

To test the potential efficiency of this alternate strategy, we turned to stochastic simulations. We first considered a “pre-coupled” model, as we had assumed previously for MORs. In this model, receptors are laterally concentrated at the active zone (with an accumulation constant K) and are activated locally upon binding of ligand (Figure S5G). We then considered an alternate “mobile” model in which receptors freely diffuse on the axon surface (Figure 5F). In this model, receptors are capable of binding ligand at all locations but become active (with activation constant K) only when present in the active zone (Figure S5H). We deployed these models on an axon profile derived from serial section electron micrographs (Figure S5I). As expected, the pre-coupled model produced a significantly larger number of ligand-receptor complexes at the active zone at all K values tested (Figure 5G). However, our data also indicate that receptors rapidly undergo phosphorylation-dependent endocytosis after ligand activation and that they do so specifically in terminals. This assures that ligand-activated MORs can couple only transiently to effectors at the presynaptic surface before they are inactivated and removed. Accordingly, effectors at the active zone sample newly formed ligand-receptor complexes rather than measuring the total concentration of ligand-receptor complexes present at the active zone. We accounted for this by including an inactivation step in the simulation and scoring independent ligand-receptor complexes at the active zone. When an inactivation step was included, the mobile model produced a greater “sampling rate” than the pre-coupled model at all K values tested and over a wide range of other parameters (Figures 5H–5J). These findings indicate that lateral mobility of receptors can indeed provide an alternate strategy for local signaling at terminals. They also indicate that, when ligand-bound receptors are rapidly inactivated at terminals, lateral diffusion offers performance that is inherently superior to that possible by pre-coupling.

DISCUSSION

The present results delineate a discrete regulated endocytic cycle operating at boutons for GPCRs, which mediates rapid removal of activated receptors specifically from the surface of terminals and re-inserts receptors both in boutons and in the axon shaft. This dynamic cycling behavior appears incompatible with the previous understanding of presynaptic GPCR cell biology, based on the paradigm of receptor immobilization at the surface of boutons. We then show, opposite to this strategy, that MOR is rapidly mobile throughout the axon surface, including at synapses. Together, these results reveal a distinct cell biology of GPCRs at the presynapse and suggest an alternate strategy for local effector control at terminals.

To our knowledge, this study is the first to examine GPCR trafficking in axons at the level of discrete membrane trafficking events and the first to directly demonstrate regulated endocytosis of any neuromodulator receptor at the presynaptic terminal. We identify a discrete population of endocytic carriers that transit receptors after local endocytosis at the presynapse, and we demonstrate receptor re-insertion to the axon surface from these carriers both in boutons and the adjacent axon shaft domain. Accordingly, this work also delineates a complete regulated endocytic membrane cycle at the presynapse that oper-

ates in parallel to the classical synaptic vesicle cycle, using separate membrane carriers and different regulation. These results add to the emerging appreciation that multiple endocytic and exocytic routes exist at the presynapse (Ashrafi et al., 2017; Hua et al., 2011; Kokotos and Cousin, 2015; Watanabe et al., 2013) and significantly advance this view by delineating an altogether separate membrane trafficking cycle for integral membrane proteins at the presynapse.

The present results also provide new insight into the organization of GPCR regulatory machinery in neurons. Many GPCRs engage a conserved mechanism after ligand-induced activation that prevents GPCRs from coupling to effectors via G proteins and subsequently drives receptor endocytosis (Gainetdinov et al., 2004; Williams et al., 2013). MORs have been shown explicitly to engage this machinery in somata and dendrites, producing acute desensitization of net MOR signaling responsiveness (Arttamangkul et al., 2018; Kliewer et al., 2019; Yousuf et al., 2015). The fact that MOR signaling at the presynapse is sustained under conditions that robustly desensitize the postsynaptic MOR response led us to anticipate that the phosphorylation-endocytosis mechanism does not operate in axons or that MORs are selectively unable to engage it in this membrane domain. The present results demonstrate that MORs indeed undergo phosphorylation-dependent endocytosis in axons but that endocytosis occurs almost exclusively at terminals and that the net degree of surface receptor depletion is small (~17%) relative to the somata, where it was previously estimated to be more than 50% (Haberstock-Debic et al., 2005). Regulated endocytosis of GPCRs in somata and dendrites has been shown to occur throughout the membrane surface at densely distributed sites (Rosendale et al., 2017). In axons, the present data show that regulated endocytosis is organized differently, occurring at sparsely distributed sites along the membrane surface and almost exclusively at terminals. We estimate a more than 15-fold bias of endocytic events at terminals when one considers that ~85% of endocytic events occur at synapses and that synapses represent approximately one-third of the total axonal length in our cultures. Some bias toward endocytosis at terminals might be expected simply based on morphology because of the increased surface area of the plasma membrane at terminals because of a larger diameter. However, based on our measurements of the increased diameter at terminals (~2-fold), we do not think that morphology alone can account for the endocytic bias. We think that this relative bias of endocytic events to sparsely distributed synaptic sites, together with the presence of a large diffusible pool of receptors on the axon surface actively replenished by the discrete vesicular cycle, enables the conserved phosphorylation-endocytosis machinery to locally inactivate receptors at terminals while maintaining the global diffusible surface pool.

These observations suggest an alternate strategy for presynaptic neuromodulation by GPCRs that is based on receptor lateral diffusion rather than immobilization. The immobilization paradigm achieves local GPCR-effector coupling by enforced proximity, a strategy that our analysis indicates is superior to lateral diffusion when receptors are not inactivated. However, in the presence of local GPCR inactivation and/or internalization, as we demonstrate here for MORs, lateral diffusion is a superior

strategy (Figure 5H). We believe that this is possible because the inherently allosteric nature of GPCR signaling, where ligand binding to receptors and receptor coupling to effectors occur in separate steps (Calebiro and Koszegi, 2019; De Lean et al., 1980; Hilger et al., 2018), enables effectors restricted at terminals to sample ligand-receptor complexes that form outside of synapses and then enter by diffusion. Such extended allostery requires ligands to have a sufficiently long residence time relative to receptor diffusion time, and we show that this constraint is met over a wide range of ligand binding affinities within the range of binding of physiological opioid peptide ligands to MORs (Figure 5I). However, we anticipate that this strategy would not be useful for GPCRs that bind physiological ligands with relatively low affinity, such as mGlu receptors that bind glutamate in the high-micromolar affinity range and, contrary to MORs, are physically concentrated at the presynaptic surface by protein scaffolding (Fisher et al., 2018). Our data also indicate that, provided that the ligand binding affinity to the GPCR is sufficiently high and that there exists an inactivation step at the terminal, lateral diffusion provides an advantageous strategy for local ligand detection at terminals over a wide range of surface receptor densities (Figure 5J). Accordingly, when one considers the key challenge of achieving local control of effectors at sparsely distributed presynaptic terminals, lateral mobility of receptors on the axon surface can provide an efficient and economical solution.

Our stochastic model tests how rapid lateral mobility of MOR is compatible with a sensitive presynaptic response, but it does not explicitly test resistance of the presynaptic response to desensitization. The reason is that the model does not include trafficking events that follow local inactivation of receptors at terminals. We believe that these later events work in concert, enabling the presynaptic MOR response to resist desensitization by maintaining a large reserve of diffusible receptors on the axon surface. It will be interesting in future studies to extend the modeling approach to include these events and more precisely assess the integrated effects of the presently defined trafficking events on presynaptic MOR signaling.

We believe that lateral diffusion and immobilization represent distinct cellular strategies for local ligand detection at terminals, with both co-existing and each offering different advantages depending on physiological context. For example, opioid peptides are able to produce significant presynaptic inhibition at low nanomolar concentrations (Pennock and Hentges, 2011), and this corresponds to few molecules at the size scale of a presynaptic terminal. Such sensitivity would approach the stochastic limit of detection based on GPCR immobilization, whereas lateral diffusion could avoid this by increasing the volume any particular terminal can sample. For ligands such as glutamate, which typically function at a higher concentration, the stochastic limit is not approached, and immobilization is likely a preferred strategy because of its kinetic advantages (Calebiro and Koszegi, 2019; Chalifoux and Carter, 2011). Lateral diffusion may also explain how some terminals are regulated by multiple GPCR types through a shared pool of presynaptic effectors (Betke et al., 2012; Pennock et al., 2012; Wu and Saggau, 1997). This would be difficult to achieve using the immobilization strategy, based on simple steric considerations, but the lateral diffusion strategy is compatible with presynaptic regulation by multiple GPCRs.

Also supporting this idea is that efficient sampling of extracellular ligands is possible even at very low surface receptor density when receptors are diffusely distributed rather than clustered (Berg and Purcell, 1977).

In conclusion, we delineate a discrete cell biology of GPCRs at the presynapse and propose an additional strategy for presynaptic ligand detection that is based on GPCR diffusion rather than immobilization and that leverages the inherent allostery of GPCR-effector coupling through G proteins. We anticipate that this alternate cell biology is relevant to a subset of GPCRs that bind cognate neuromodulators with high affinity relative to conventional synaptic neurotransmitters. Our results also identify a parallel regulated endocytic cycle operating at the presynaptic terminal to mediate neuromodulator receptor trafficking, separate from the synaptic vesicle cycle that mediates neurotransmitter packaging and release. This parallel regulated endocytic membrane cycle, in addition to enabling an alternate strategy for GPCR signaling at terminals, adds to the growing recognition of remarkable diversity and specificity of membrane traffic at the presynapse.

STAR★METHODS

Detailed methods are provided in the online version of this paper and include the following:

- KEY RESOURCES TABLE
- LEAD CONTACT AND MATERIALS AVAILABILITY
- EXPERIMENTAL MODEL AND SUBJECT DETAILS
 - Primary rat neurons culture
- METHOD DETAILS
 - cDNA constructs
 - Anti-GFP nanobody expression, purification, and conjugation
 - Widefield imaging
 - Spinning disc confocal, dSTORM and SIM imaging
 - Photoactivation
 - Oblique illumination
 - Statistics
 - Quantitative image analysis
 - Modeling
- DATA AND CODE AVAILABILITY

SUPPLEMENTAL INFORMATION

Supplemental Information can be found online at <https://doi.org/10.1016/j.neuron.2019.11.016>.

ACKNOWLEDGMENTS

We thank Robert Edwards and members of his laboratory for discussions and reagents, David Perrais for valuable discussions and technical advice, and Stefan Schulz for valuable discussions and important reagents. We thank Roger Nicoll, Tim Ryan, John Williams, Gregory Scherrer, and members of the von Zastrow laboratory for valuable discussions and suggestions. Some of the imaging experiments were carried out in the UCSF Nikon Imaging Center directed by DeLaine Larsen. This study was supported by research grants from the NIH/NIDA (DA010711 and DA012864). M.S. was supported by the Swiss National Science Foundation (P2EZP3_152173 and P300PA_164712).

D.J. received support from the UCSF Program for Breakthrough Biomedical Research. S.A. received support from NIH/ NIDA DA048136.

AUTHOR CONTRIBUTIONS

D.J. and M.v.Z. conceived the experiments and wrote the manuscript. D.J., H.L.Z., and E.H. performed the experiments and analyzed the data. M.S. and S.A. provided essential reagents. J.-B.S., T.M.B., and T.J.S. provided software and support for data analysis and interpretation.

DECLARATION OF INTERESTS

The authors declare no competing interests.

Received: February 8, 2019

Revised: August 2, 2019

Accepted: November 11, 2019

Published: December 11, 2019

REFERENCES

Alvarez, V.A., Arttamangkul, S., Dang, V., Salem, A., Whistler, J.L., Von Zastrow, M., Grandy, D.K., and Williams, J.T. (2002). μ -Opioid receptors: Ligand-dependent activation of potassium conductance, desensitization, and internalization. *J. Neurosci.* *22*, 5769–5776.

Arttamangkul, S., Alvarez-Maubecin, V., Thomas, G., Williams, J.T., and Grandy, D.K. (2000). Binding and internalization of fluorescent opioid peptide conjugates in living cells. *Mol. Pharmacol.* *58*, 1570–1580.

Arttamangkul, S., Heinz, D.A., Bunzow, J.R., Song, X., and Williams, J.T. (2018). Cellular tolerance at the μ -opioid receptor is phosphorylation dependent. *eLife* *7*, e34989.

Ashrafi, G., Wu, Z., Farrell, R.J., and Ryan, T.A. (2017). GLUT4 Mobilization Supports Energetic Demands of Active Synapses. *Neuron* *93*, 606–615.e3.

Ball, G., Demmerle, J., Kaufmann, R., Davis, I., Dobbie, I.M., and Schermelleh, L. (2016). Erratum: SIMcheck: a Toolbox for Successful Super-resolution Structured Illumination Microscopy. *Sci. Rep.* *6*, 20754.

Banker, G., and Goslin, K. (1998). *Culturing Nerve Cells*, Second Edition, Bradford.

Bartol, T.M., Bromer, C., Kinney, J., Chirillo, M.A., Bourne, J.N., Harris, K.M., and Sejnowski, T.J. (2015a). Nanoconnectomic upper bound on the variability of synaptic plasticity. *eLife* *4*, e10778.

Bartol, T.M., Keller, D.X., Kinney, J.P., Bajaj, C.L., Harris, K.M., Sejnowski, T.J., and Kennedy, M.B. (2015b). Computational reconstitution of spine calcium transients from individual proteins. *Front. Synaptic Neurosci.* *7*, 17.

Berg, H.C., and Purcell, E.M. (1977). Physics of chemoreception. *Biophys. J.* *20*, 193–219.

Betke, K.M., Wells, C.A., and Hamm, H.E. (2012). GPCR mediated regulation of synaptic transmission. *Prog. Neurobiol.* *96*, 304–321.

Birdsong, W.T., Arttamangkul, S., Clark, M.J., Cheng, K., Rice, K.C., Traynor, J.R., and Williams, J.T. (2013). Increased agonist affinity at the μ -opioid receptor induced by prolonged agonist exposure. *J. Neurosci.* *33*, 4118–4127.

Boudin, H., Doan, A., Xia, J., Shigemoto, R., Hagan, R.L., Worley, P., and Craig, A.M. (2000). Presynaptic clustering of mGluR7a requires the PICK1 PDZ domain binding site. *Neuron* *28*, 485–497.

Brown, D.A., and Sihra, T.S. (2008). Presynaptic signaling by heterotrimeric G-proteins. *Handb. Exp. Pharmacol.* *184*, 207–260.

Calebiro, D., and Koszegi, Z. (2019). The subcellular dynamics of GPCR signaling. *Mol. Cell. Endocrinol.* *483*, 24–30.

Chalifoux, J.R., and Carter, A.G. (2011). GABAB receptor modulation of synaptic function. *Curr. Opin. Neurobiol.* *21*, 339–344.

Chéreau, R., Saraceno, G.E., Angibaud, J., Cattaert, D., and Nägerl, U.V. (2017). Superresolution imaging reveals activity-dependent plasticity of axon morphology linked to changes in action potential conduction velocity. *Proc. Natl. Acad. Sci. USA* *114*, 1401–1406.

Choy, R.W.-Y., Park, M., Temkin, P., Herring, B.E., Marley, A., Nicoll, R.A., and von Zastrow, M. (2014). Retromer mediates a discrete route of local membrane delivery to dendrites. *Neuron* *82*, 55–62.

Corder, G., Castro, D.C., Bruchas, M.R., and Scherrer, G. (2018). Endogenous and Exogenous Opioids in Pain. *Annu. Rev. Neurosci.* *41*, 453–473.

Corti, C., Aldegheri, L., Somogyi, P., and Ferraguti, F. (2002). Distribution and synaptic localisation of the metabotropic glutamate receptor 4 (mGluR4) in the rodent CNS. *Neuroscience* *110*, 403–420.

Dalezios, Y., Luján, R., Shigemoto, R., Roberts, J.D.B., and Somogyi, P. (2002). Enrichment of mGluR7a in the presynaptic active zones of GABAergic and non-GABAergic terminals on interneurons in the rat somatosensory cortex. *Cereb. Cortex* *12*, 961–974.

Darcq, E., and Kieffer, B.L. (2018). Opioid receptors: drivers to addiction? *Nat. Rev. Neurosci.* *19*, 499–514.

De Lean, A., Stadel, J.M., and Lefkowitz, R.J. (1980). A ternary complex model explains the agonist-specific binding properties of the adenylate cyclase-coupled beta-adrenergic receptor. *J. Biol. Chem.* *255*, 7108–7117.

Dudok, B., Barna, L., Ledri, M., Szabó, S.I., Szabadits, E., Pintér, B., Woodhams, S.G., Henstridge, C.M., Balla, G.Y., Nyilas, R., et al. (2015). Cell-specific STORM super-resolution imaging reveals nanoscale organization of cannabinoid signaling. *Nat. Neurosci.* *18*, 75–86.

Eichel, K., Jullié, D., and von Zastrow, M. (2016). β -Arrestin drives MAP kinase signalling from clathrin-coated structures after GPCR dissociation. *Nat. Cell Biol.* *18*, 303–310.

Fisher, N.M., Seto, M., Lindsley, C.W., and Niswender, C.M. (2018). Metabotropic Glutamate Receptor 7: A New Therapeutic Target in Neurodevelopmental Disorders. *Front. Mol. Neurosci.* *11*, 387.

Fyfe, L.W., Cleary, D.R., Macey, T.A., Morgan, M.M., and Ingram, S.L. (2010). Tolerance to the antinociceptive effect of morphine in the absence of short-term presynaptic desensitization in rat periaqueductal gray neurons. *J. Pharmacol. Exp. Ther.* *335*, 674–680.

Gainetdinov, R.R., Premont, R.T., Bohn, L.M., Lefkowitz, R.J., and Caron, M.G. (2004). Desensitization of G protein-coupled receptors and neuronal functions. *Annu. Rev. Neurosci.* *27*, 107–144.

Giannone, G., Hosy, E., Sibarita, J.-B., Choquet, D., and Cognet, L. (2013). High-content super-resolution imaging of live cell by uPAINT. *Methods Mol. Biol.* *950*, 95–110.

Haas, K.T., Compans, B., Letellier, M., Bartol, T.M., Grillo-Bosch, D., Sejnowski, T.J., Sainlos, M., Choquet, D., Thoumine, O., and Hosy, E. (2018). Pre-post synaptic alignment through neuroligin-1 tunes synaptic transmission efficiency. *eLife* *7*, e31755.

Haberstock-Debic, H., Kim, K.-A., Yu, Y.J., and von Zastrow, M. (2005). Morphine promotes rapid, arrestin-dependent endocytosis of μ -opioid receptors in striatal neurons. *J. Neurosci.* *25*, 7847–7857.

Herlitze, S., Garcia, D.E., Mackie, K., Hille, B., Scheuer, T., and Catterall, W.A. (1996). Modulation of Ca²⁺ channels by G-protein beta gamma subunits. *Nature* *380*, 258–262.

Hilger, D., Masureel, M., and Kobilka, B.K. (2018). Structure and dynamics of GPCR signaling complexes. *Nat. Struct. Mol. Biol.* *25*, 4–12.

Hua, Z., Leal-Ortiz, S., Foss, S.M., Waites, C.L., Garner, C.C., Voglmaier, S.M., and Edwards, R.H. (2011). v-SNARE composition distinguishes synaptic vesicle pools. *Neuron* *71*, 474–487.

Jullié, D., Choquet, D., and Perrais, D. (2014). Recycling endosomes undergo rapid closure of a fusion pore on exocytosis in neuronal dendrites. *J. Neurosci.* *34*, 11106–11118.

Just, S., Illing, S., Trester-Zedlitz, M., Lau, E.K., Kotowski, S.J., Miess, E., Mann, A., Doll, C., Trinidad, J.C., Burlingame, A.L., et al. (2013). Differentiation of opioid drug effects by hierarchical multi-site phosphorylation. *Mol. Pharmacol.* *83*, 633–639.

Kaech, S., and Banker, G. (2006). Culturing hippocampal neurons. *Nat. Protoc.* *1*, 2406–2415.

- Keckhar, A., Nair, D., Heilemann, M., Choquet, D., and Sibarita, J.B. (2013). Real-time analysis and visualization for single-molecule based super-resolution microscopy. *PLoS One* 8, e62918.
- Kieffer, B.L., and Evans, C.J. (2009). Opioid receptors: from binding sites to visible molecules in vivo. *Neuropharmacology* 56 (Suppl 1), 205–212.
- Kinney, J.P., Spacek, J., Bartol, T.M., Bajaj, C.L., Harris, K.M., and Sejnowski, T.J. (2013). Extracellular sheets and tunnels modulate glutamate diffusion in hippocampal neuropil. *J. Comp. Neurol.* 521, 448–464.
- Kliwewer, A., Schmiedel, F., Sianati, S., Bailey, A., Bateman, J.T., Levitt, E.S., Williams, J.T., Christie, M.J., and Schulz, S. (2019). Phosphorylation-deficient G-protein-biased μ -opioid receptors improve analgesia and diminish tolerance but worsen opioid side effects. *Nat. Commun.* 10, 367.
- Kokotos, A.C., and Cousin, M.A. (2015). Synaptic vesicle generation from central nerve terminal endosomes. *Traffic* 16, 229–240.
- Kubala, M.H., Kovtun, O., Alexandrov, K., and Collins, B.M. (2010). Structural and thermodynamic analysis of the GFP:GFP-nanobody complex. *Protein Sci.* 19, 2389–2401.
- Laviv, T., Vertkin, I., Berdichevsky, Y., Fogel, H., Riven, I., Bettler, B., Slesinger, P.A., and Slutsky, I. (2011). Compartmentalization of the GABAB receptor signaling complex is required for presynaptic inhibition at hippocampal synapses. *J. Neurosci.* 31, 12523–12532.
- Lowe, J.D., and Bailey, C.P. (2015). Functional selectivity and time-dependence of μ -opioid receptor desensitization at nerve terminals in the mouse ventral tegmental area. *Br. J. Pharmacol.* 172, 469–481.
- Lowe, J.D., Sanderson, H.S., Cooke, A.E., Ostovar, M., Tsisanova, E., Withey, S.L., Chavkin, C., Husbands, S.M., Kelly, E., Henderson, G., and Bailey, C.P. (2015). Role of G Protein-Coupled Receptor Kinases 2 and 3 in μ -Opioid Receptor Desensitization and Internalization. *Mol. Pharmacol.* 88, 347–356.
- Lupp, A., Richter, N., Doll, C., Nagel, F., and Schulz, S. (2011). UMB-3, a novel rabbit monoclonal antibody, for assessing μ -opioid receptor expression in mouse, rat and human formalin-fixed and paraffin-embedded tissues. *Regul. Pept.* 167, 9–13.
- Manley, S., Gillette, J.M., Patterson, G.H., Shroff, H., Hess, H.F., Betzig, E., and Lippincott-Schwartz, J. (2008). High-density mapping of single-molecule trajectories with photoactivated localization microscopy. *Nat. Methods* 5, 155–157.
- McKinney, S.A., Murphy, C.S., Hazelwood, K.L., Davidson, M.W., and Looger, L.L. (2009). A bright and photostable photoconvertible fluorescent protein. *Nat. Methods* 6, 131–133.
- Mengual, E., and Pickel, V.M. (2002). Ultrastructural immunocytochemical localization of the dopamine D2 receptor and tyrosine hydroxylase in the rat ventral pallidum. *Synapse* 43, 151–162.
- Merrifield, C.J., Perrais, D., and Zenisek, D. (2005). Coupling between clathrin-coated-pit invagination, cortactin recruitment, and membrane scission observed in live cells. *Cell* 121, 593–606.
- Nair, D., Hosy, E., Petersen, J.D., Constals, A., Giannone, G., Choquet, D., and Sibarita, J.-B. (2013). Super-resolution imaging reveals that AMPA receptors inside synapses are dynamically organized in nanodomains regulated by PSD95. *J. Neurosci.* 33, 13204–13224.
- Nyíri, G., Cserép, C., Szabadits, E., Mackie, K., and Freund, T.F. (2005). CB1 cannabinoid receptors are enriched in the perisynaptic annulus and on preterminal segments of hippocampal GABAergic axons. *Neuroscience* 136, 811–822.
- Pelkey, K.A., Topolnik, L., Yuan, X.-Q., Lacaille, J.-C., and McBain, C.J. (2008). State-dependent cAMP sensitivity of presynaptic function underlies metaplasticity in a hippocampal feedforward inhibitory circuit. *Neuron* 60, 980–987.
- Pennock, R.L., Dicken, M.S., and Hentges, S.T. (2012). Multiple inhibitory G-protein-coupled receptors resist acute desensitization in the presynaptic but not postsynaptic compartments of neurons. *J. Neurosci.* 32, 10192–10200.
- Pennock, R.L., and Hentges, S.T. (2011). Differential expression and sensitivity of presynaptic and postsynaptic opioid receptors regulating hypothalamic proopiomelanocortin neurons. *J. Neurosci.* 31, 281–288.
- Pfenninger, K.H. (2009). Plasma membrane expansion: a neuron's Herculean task. *Nat. Rev. Neurosci.* 10, 251–261.
- Rosendale, M., Jullié, D., Choquet, D., and Perrais, D. (2017). Spatial and Temporal Regulation of Receptor Endocytosis in Neuronal Dendrites Revealed by Imaging of Single Vesicle Formation. *Cell Rep.* 18, 1840–1847.
- Rossier, O., Oceau, V., Sibarita, J.-B., Leduc, C., Tessier, B., Nair, D., Gatterdam, V., Destaing, O., Albigès-Rizo, C., Tampé, R., et al. (2012). Integrins $\beta 1$ and $\beta 3$ exhibit distinct dynamic nanoscale organizations inside focal adhesions. *Nat. Cell Biol.* 14, 1057–1067.
- Sankaranarayanan, S., De Angelis, D., Rothman, J.E., and Ryan, T.A. (2000). The use of pHluorins for optical measurements of presynaptic activity. *Biophys. J.* 79, 2199–2208.
- Santos, M.S., Park, C.K., Foss, S.M., Li, H., and Voglmaier, S.M. (2013). Sorting of the vesicular GABA transporter to functional vesicle pools by an atypical dileucine-like motif. *J. Neurosci.* 33, 10634–10646.
- Sesack, S.R., Aoki, C., and Pickel, V.M. (1994). Ultrastructural localization of D2 receptor-like immunoreactivity in midbrain dopamine neurons and their striatal targets. *J. Neurosci.* 14, 88–106.
- Shigemoto, R., Kulik, A., Roberts, J.D., Ohishi, H., Nusser, Z., Kaneko, T., and Somogyi, P. (1996). Target-cell-specific concentration of a metabotropic glutamate receptor in the presynaptic active zone. *Nature* 381, 523–525.
- Somogyi, P., Dalezios, Y., Luján, R., Roberts, J.D.B., Watanabe, M., and Shigemoto, R. (2003). High level of mGluR7 in the presynaptic active zones of select populations of GABAergic terminals innervating interneurons in the rat hippocampus. *Eur. J. Neurosci.* 17, 2503–2520.
- Stoeber, M., Jullié, D., Lobingier, B.T., Laeremans, T., Steyaert, J., Schiller, P.W., Manglik, A., and von Zastrow, M. (2018). A Genetically Encoded Biosensor Reveals Location Bias of Opioid Drug Action. *Neuron* 98, 963–976.e5.
- Svingos, A.L., Moriwaki, A., Wang, J.B., Uhl, G.R., and Pickel, V.M. (1997). μ -Opioid receptors are localized to extrasynaptic plasma membranes of GABAergic neurons and their targets in the rat nucleus accumbens. *J. Neurosci.* 17, 2585–2594.
- Takamori, S., Holt, M., Stenius, K., Lemke, E.A., Grønborg, M., Riedel, D., Urlaub, H., Schenck, S., Brügger, B., Ringler, P., et al. (2006). Molecular anatomy of a trafficking organelle. *Cell* 127, 831–846.
- Vargas, K.J., Terunuma, M., Tello, J.A., Pangalos, M.N., Moss, S.J., and Couve, A. (2008). The availability of surface GABA B receptors is independent of gamma-aminobutyric acid but controlled by glutamate in central neurons. *J. Biol. Chem.* 283, 24641–24648.
- Vazquez-Sanchez, S., Bobeldijk, S., Dekker, M.P., van Keimpema, L., and van Weering, J.R.T. (2018). VPS35 depletion does not impair presynaptic structure and function. *Sci. Rep.* 8, 2996.
- Vigot, R., Barbieri, S., Bräuner-Osborne, H., Turecek, R., Shigemoto, R., Zhang, Y.-P., Luján, R., Jacobson, L.H., Biermann, B., Fritschy, J.-M., et al. (2006). Differential compartmentalization and distinct functions of GABAB receptor variants. *Neuron* 50, 589–601.
- Voglmaier, S.M., Kam, K., Yang, H., Fortin, D.L., Hua, Z., Nicoll, R.A., and Edwards, R.H. (2006). Distinct endocytic pathways control the rate and extent of synaptic vesicle protein recycling. *Neuron* 51, 71–84.
- Wang, H., Moriwaki, A., Wang, J.B., Uhl, G.R., and Pickel, V.M. (1996). Ultrastructural immunocytochemical localization of μ opioid receptors and Leu5-enkephalin in the patch compartment of the rat caudate-putamen nucleus. *J. Comp. Neurol.* 375, 659–674.
- Watanabe, S., Rost, B.R., Camacho-Pérez, M., Davis, M.W., Söhl-Kielczynski, B., Rosenmund, C., and Jørgensen, E.M. (2013). Ultrafast endocytosis at mouse hippocampal synapses. *Nature* 504, 242–247.
- Werling, L.L., Brown, S.R., and Cox, B.M. (1987). Opioid receptor regulation of the release of norepinephrine in brain. *Neuropharmacology* 26 (7B), 987–996.
- Wetherington, J.P., and Lambert, N.A. (2002). Differential desensitization of responses mediated by presynaptic and postsynaptic A1 adenosine receptors. *J. Neurosci.* 22, 1248–1255.

Whistler, J.L., and von Zastrow, M. (1998). Morphine-activated opioid receptors elude desensitization by beta-arrestin. *Proc. Natl. Acad. Sci. USA* *95*, 9914–9919.

Wilding, T.J., Womack, M.D., and McCleskey, E.W. (1995). Fast, local signal transduction between the mu opioid receptor and Ca²⁺ channels. *J. Neurosci.* *15*, 4124–4132.

Williams, J.T., Ingram, S.L., Henderson, G., Chavkin, C., von Zastrow, M., Schulz, S., Koch, T., Evans, C.J., and Christie, M.J. (2013). Regulation of μ -opioid receptors: desensitization, phosphorylation, internalization, and tolerance. *Pharmacol. Rev.* *65*, 223–254.

Wu, L.G., and Saggau, P. (1997). Presynaptic inhibition of elicited neurotransmitter release. *Trends Neurosci.* *20*, 204–212.

Yousuf, A., Miess, E., Sianati, S., Du, Y.-P., Schulz, S., and Christie, M.J. (2015). Role of Phosphorylation Sites in Desensitization of μ -Opioid Receptor. *Mol. Pharmacol.* *88*, 825–835.

Yu, Y.J., Dhavan, R., Chevalier, M.W., Yudowski, G.A., and von Zastrow, M. (2010). Rapid delivery of internalized signaling receptors to the somatodendritic surface by sequence-specific local insertion. *J. Neurosci.* *30*, 11703–11714.

Zhang, J., Ferguson, S.S., Barak, L.S., Bodduluri, S.R., Laporte, S.A., Law, P.Y., and Caron, M.G. (1998). Role for G protein-coupled receptor kinase in agonist-specific regulation of mu-opioid receptor responsiveness. *Proc. Natl. Acad. Sci. USA* *95*, 7157–7162.

STAR★METHODS

KEY RESOURCES TABLE

REAGENT or RESOURCE	SOURCE	IDENTIFIER
Antibodies		
Mouse anti-FLAG (M1)	Sigma	Cat# F-3040; RRID: AB_439712
Anti-HA Alexa 488	Thermo Fisher Scientific	Cat# A-21287, RRID: AB_2535829
Anti-HA Alexa-594	Thermo Fisher Scientific	Cat# A-21288, RRID: AB_2535830
Donkey anti-Mouse IgG Secondary Antibody, Alexa Fluor 488	Thermo Fisher Scientific	Cat# A-21202, RRID: AB_141607
Donkey anti-Mouse IgG Secondary Antibody, Alexa Fluor 555	Thermo Fisher Scientific	Cat# A31570, RRID: AB_2536180
Donkey anti-Goat IgG Secondary Antibody, Alexa Fluor 647	Thermo Fisher Scientific	Cat# A21447, RRID: AB_2535864
Donkey anti-Guinea Pig IgG Secondary Antibody, Cy3	Jackson ImmunoResearch Labs	Cat# 706-165-148, RRID: AB_2340460
Donkey anti-Guinea Pig IgG Secondary Antibody, Alexa Fluor 488	Thermo Fisher Scientific	Cat# A-11073, RRID: AB_142018
Goat anti-Rabbit IgG Secondary Antibody, Alexa Fluor 647	Thermo Fisher Scientific	Cat# A-21245, RRID: AB_2535813 Cat# A-21244, RRID: AB_2535812
Goat anti-Rabbit IgG Secondary Antibody, Alexa Fluor 488	Thermo Fisher Scientific	Cat# A-21206, RRID: AB_141708
Rabbit anti-MOR (UMB3)	Abcam	Cat# ab134054
Goat anti-VPS35	Novus	Cat# NB100-1397, RRID: AB_2257186
Guinea pig anti-VGLUT2	Millipore	Cat# AB2251-I, RRID: AB_2665454
Mouse anti-SV2	DSHB	Cat# SV2, RRID: AB_2315387
Guinea Pig anti-Parvalbumin	Synaptic Systems	Cat# 195 004, RRID: AB_2156476
Mouse anti-GAD67	Millipore	Cat# MAB5406, RRID: AB_2278725
Chemicals, Peptides, and Recombinant Proteins		
DAMGO, [D-Ala ² , N-Me-Phe ⁴ , Gly ⁵ -ol]-Enkephalin acetate salt	Sigma-Aldrich	E7384
dermorphin-A488	Arttamangkul et al., 2000	N/A
Alexa Fluor 647 Protein Labeling Kit	Thermo Fisher Scientific	Cat# A20173
Alexa Fluor 488 Protein Labeling Kit	Thermo Fisher Scientific	Cat# A20173
Atto647N NHS-ester Protein labeling kit	ATTO-TEC	Cat# AD 647N-31
Compound 101	Tocris	Cat# 5642
Tetrodotoxin (TTX)	Abcam	Cat# ab120054
Amiloride	Sigma-Aldrich	Cat# A7410
Experimental Models: Organisms/Strains		
Rat: Sprague Dawley	Charles River Janvier Labs	N/A
Recombinant DNA		
pCAGGS/SE: signal sequence FLAG (SSF)-MOR, murine	Stoeber et al., 2018	N/A
pCAGGS/SE: SSF-MOR-EGFP	Stoeber et al., 2018	N/A
pCAGGS/SE: SSF-MOR-PAGFP	This study	N/A
pCAGGS/SE: SSF-MOR-mEos2	This study	N/A
pCAGGS/SE: HA-MOR	This study	N/A
pCAGGS/SE: SEP-MOR	This study	N/A

(Continued on next page)

Continued

REAGENT or RESOURCE	SOURCE	IDENTIFIER
pCAGGS/SE: S/T to A MOR	This study	N/A
pCAGGS/SE: VPS29-GFP	Choy et al., 2014	N/A
pCAGGS/SE: VPS29-GFP	Choy et al., 2014	N/A
pCAGGS/SE: synaptophysin-mCherry	Hua et al., 2011	N/A
pCAGGS/SE: VGAT-SEP	Santos et al., 2013	N/A
pcDNA3.1: β -arrestin2-GFP	Eichel et al., 2016	N/A
pCAGGS/SE: VAMP2-SEP	Voglmaier et al., 2006	N/A
Software and Algorithms		
MATLAB	MathWorks	R2014b
Metamorph	Molecular Devices	7.7
MCell	https://mcell.org/	3.3
CellBlender	https://mcell.org/	1.1
Blender	http://www.blender.org	2.77a
Excel	Microsoft	16.11.1

LEAD CONTACT AND MATERIALS AVAILABILITY

Further information and requests for resources and reagents should be directed to and will be fulfilled by the Lead Contact Mark von Zastrow (mark@vzlab.org). All unique/stable reagents generated in this study are available from the Lead Contact without restriction.

EXPERIMENTAL MODEL AND SUBJECT DETAILS**Primary rat neurons culture**

Neurons were prepared from embryonic day 18 Sprague-Dawley rats. All procedures were performed according to the National Institutes of Health Guide for Care and Use of Laboratory Animals and approved by the University of California San Francisco Institutional Animal Care and Use Committee. Briefly, the striatum, including the caudate-putamen and nucleus accumbens, hippocampi and habenula were identified ([Banker and Goslin, 1998](#)). The structures were dissected in ice cold Hank's buffered saline solution Calcium/magnesium/phenol red free (University of California, San Francisco, Cell Culture Facility). Structures were dissociated in 1x trypsin/EDTA (University of California, San Francisco, Cell Culture Facility) for 15 min at 37°C. Cells were washed in GIBCO Dulbecco's modified Eagle's medium (Invitrogen) supplemented with 10% fetal bovine serum (University of California, San Francisco, Cell Culture Facility) and 30mM HEPES, then mechanically separated with a flame-polished Pasteur pipette. When nucleofected, striatal and habenula neurons were transfected using manufacturer's instructions (Rat Neuron Nucleofector Kit, Lonza) for rat hippocampal neurons before plating. Cells were plated on poly-D-lysine coated 35mm glass bottom dishes (Matek) in GIBCO Dulbecco's modified Eagle's medium supplemented with 10% fetal bovine serum. Media was exchanged 1-4 days after plating for Neurobasal (Invitrogen) supplemented with Glutamax 1x (Invitrogen) and B27 1x (Thermo Fisher). For dSTORM imaging, hippocampal cultures were prepared according to the Banker protocol ([Kaeck and Banker, 2006](#)), and as detailed in [Haas et al. \(2018\)](#). Half of the culture media was exchanged every week with fresh, equilibrated media. Cytosine arabinosine 2 μ M (Sigma-Aldrich) was added at 8 DIV. Lipofectamine 2000 (Thermo Fisher) transfection was performed on DIV 8, using 1 μ l of lipofectamine and 1 μ g DNA in 1ml of media per 35mm imaging dish, and media was exchanged 6 hours later. Cells were maintained in a humidified incubator with 5% CO₂ at 37°C and imaged after 14-21 days *in vitro*. All experiments were performed on at least 2 independent cultures.

METHOD DETAILS**cDNA constructs**

To generate SSF-MOR-mEos2, SSF-MOR and mEos2 were amplified by PCR and inserted into pCAGGS-SE by multiway ligation using SacI, EcoRI and AgeI sites. SSF-MOR and PAGFP were amplified by PCR and inserted into pCAGGS-SE by multiway ligation using SacI, KpnI and EcoRI sites to generate SSF-MOR-PAGFP. Signal sequence HA-MOR (simplified as HA-MOR in the manuscript) was amplified by PCR and inserted into pCAGGS-SE by ligation using SacI and KpnI sites. SEP-MOR as well as the S/T to A MOR mutant were amplified by PCR and inserted into pCAGGS-SE using EcoRI and XhoI sites.

Anti-GFP nanobody expression, purification, and conjugation

The pOPINE plasmid encoding the GFP nanobody (GFP-Nb) with a C-terminal 6x-His tag (Kubala et al., 2010) was transformed into BL21-Gold (DE3) Competent Cells. Cells were grown at 37°C in TB medium. Protein expression was induced with 0.5mM imidazole and culture incubated for 16h at 20°C. Cells were harvested and pellet snap frozen and stored at –80°C. Pellet was thawed and re-suspended in breaking buffer B1 (50 mM HEPES, 500mM NaCl, 10% glycerol, 5mM DTT, 10mM imidazole, protease inhibitors, pH 7.5, supplemented with Complete EDTA-free protease inhibitor cocktail (Sigma-Aldrich) and lysed by sonication. Cell debris were removed by centrifugation for 30 min, 11150 g at 4°C. Cleared lysate was loaded onto a nickel-Sepharose column (His SpinTrap, GE Healthcare). Column was washed with buffer B1 followed by wash with B1 containing 40 mM imidazole, and eluted with 250 mM imidazole. Purified GFP-Nb was shown to be more than 95% pure by SDS-PAGE/Coomassie. Protein containing fractions were pooled and concentrated using Amicon Ultra centrifugal filter units MWCO 10kDa. Labeling of purified GFP-Nb with ATTO 647N NHS-ester (ATTO-TEC) was performed according to the manufacturer's procedures. In brief, labeling reaction was performed with 3-fold molar excess of dye to protein for 1h at RT in the presence of 10mM NaHCO₃. Separation of labeled GFP-Nb from unbound dye and buffer exchange was performed in size-exclusion columns (Sephadex G-25, GE Healthcare Life Sciences). The resulting ATTO647-Nb labeling ratio was determined by spectrofluorometric measurement. On average, GFP-Nb was labeled 0.6 dye molecules.

Widefield imaging

Imaging of presynaptic activity as well as endocytosis of SEP-MOR experiments were performed on a Nikon TE-2000 inverted microscope equipped with a S Fluor 40x 1.30 NA objective, a Bioptechs objective warmer and an Andor iXon EM+ EMCCD camera. Illumination, perfusion and electrical field stimulation devices were custom built. Briefly, an insert was 3D printed and equipped with two platinum wires distant of 1cm used for field stimulation. Live cell imaging was performed in HEPES buffered saline solution (HBS) adjusted to pH 7.4 containing, in mM: NaCl 120, KCl 2, CaCl₂ 2, MgCl₂ 2, Glucose 5, HEPES 10 and osmolarity was adjusted to 270mOsm. This insert left a dead volume of 300µl inside the imaging dish and was used to perfuse solutions with a debit of 1.5ml/min. This perfusion system was used to perfuse HBS, HBS + 10µM DAMGO, calcium free HBS or ammonium chloride solution (HBS containing 50mM NH₄Cl with NaCl adjusted to 80mM). Widefield illumination in the green channel was controlled and synchronized with an Arduino uno, with a blue LED replacing the mercury bulb of a Nikon lamp and an appropriate combination of filters and dichroic mirror. For imaging in the red channel, widefield illumination was performed with a micrometer-guided illuminator (Nikon) and a 543nm HeNe laser (Spectra Physics) and an appropriate set of filters and dichroic mirror. To monitor SEP-MOR endocytosis in lipofectamine transfected MSNs, syp-mCh marked axons were imaged at 1Hz and continuously perfused with HBS, HBS+10µM DAMGO or ammonium chloride solution as illustrated. To monitor synaptic vesicle exocytosis, MSNs were transfected with SSF-MOR together with VGAT-SEP using lipofectamine, VGAT-SEP only was nucleofected for imaging of presynaptic activity in calcium free condition. Axons of neurons expressing SSF-MOR were stained for 10 min with M1-Alexa-555 conjugated antibody (1/1000) before imaging to confirm receptor expression. Same approach was used for the S/T to A MOR mutant. Electrical stimulation (10 action potentials at 10hz, 10V/cm, once every minute) was controlled with an arduino uno (Arduino) to synchronize the stimulation with the acquisition. Neurons were imaged at 1Hz and perfused with the different solutions as indicated. Ammonium chloride solution was added at the end of the acquisition. Same protocol was used with habenula neurons nucleofected with VAMP2-SEP only, with a stimulation protocol of 20 action potentials at 10Hz every minute.

Spinning disc confocal, dSTORM and SIM imaging

To localize endogenous proteins in fixed cells, the same protocol was used as follows, with different combinations of primary and secondary antibodies as indicated. Cultured neurons were fixed and permeabilized for 15 min with methanol 100% at –20°C. Cells were washed 3 times with phosphate buffered saline solution (PBS) and blocked for 1 hour in PBS-3% normal donkey serum (PBS-NDS). Cells were incubated with primary antibodies diluted in PBS-NDS overnight at 4°C, rinsed 3 times with PBS-NDS, and incubated with secondary antibodies diluted 1/1000 (except when specified) in PBS-NDS for 30 min. After 3 washes with PBS-NDS followed by 3 washes with PBS, cells were directly imaged in PBS.

To evaluate the degree of MOR expression, experiments were performed in parallel on different neuron cultures prepared from the same dissection (striatal, hippocampal, habenula, SSF-MOR + syp-mCh electroporated MSNs, SEP-MOR + syp-mCh transfected MSNs using lipofectamine). Antibodies were rabbit anti-MOR (UMB3) 1/500 revealed by goat anti-rabbit-Alexa647. Cells were then imaged at room temperature on a Nikon Ti-E equipped with a Yokogawa CSU-22 spinning disc head. Microscope was equipped with a Photometrics Evolve Delta camera and a temperature-, humidity- and CO₂-controlled Okolab enclosure Bold Line incubator. 488nm, 568nm and 640nm Coherent OBIS lasers were used as light sources and 0.2µm Zstacks acquired with an Apo TIRF 60x 1.40 NA objective.

For the accumulation index experiments to test the effect of Cmpd101 on endogenous MOR distribution in habenula neurons axons, cells were preincubated with Cmpd101 30 µM or DMSO vehicle 0.06% in culture media at 37°C 5% CO₂ for 10 min, and DAMGO 10 µM was added depending on the condition for another 20 min in the incubator. Antibodies were UMB3 1/500 + mouse anti-SV2 1/500 revealed by donkey anti-rabbit-Alexa488 + donkey anti-mouse-Alexa555, cells were imaged using the spinning disc confocal as described previously.

For the accumulation index experiments to test the effect of naloxone, habenula neurons were incubated at 37°C 5% CO₂ in culture media with DAMGO 100nM for 20 min, naloxone 10 μM for 30 min, or DAMGO 100nM for 20 min followed by naloxone 10 μM for 30 min. Antibodies were UMB3 1/500 + mouse anti-SV2 1/500 revealed by donkey anti-rabbit-Alexa488 + donkey anti-mouse-Alexa555, cells were imaged using the spinning disc confocal as described previously.

To study the distribution of endogenous MOR relative to synapses, habenula neurons were incubated for 20 min with DAMGO 10 μM in culture media at 37°C 5% CO₂ or fixed directly. Antibodies were UMB3 1/500 + guinea pig anti-VGLUT2 1/1000 revealed by donkey anti-rabbit-Alexa488 + donkey anti-guinea pig-Cy3, cells were imaged using the spinning disc confocal as described previously.

To study the colocalization of MOR-containing endosomes with retromer, habenula neurons were incubated 20 min with DAMGO 10 μM in culture media at 37°C 5% CO₂. Antibodies were UMB3 1/500 + guinea pig anti-VGLUT2 1/1000 + goat anti-VPS35 1/500 revealed by donkey anti-rabbit-Alexa488 + donkey anti-guinea pig-Cy3 + donkey anti-goat-Alexa647. Cells were imaged using the spinning disc confocal as described previously or using a DeltaVision OMX SR imaging system with a 60x 1.49 NA TIRF apo objective for the SIM imaging. Image quality was checked using the SIMCheck plugin (Ball et al., 2016) running on the imageJ environment.

To study the distribution of MOR in axons of hippocampal neurons using dSTORM, hippocampal neurons were stained with UMB3 1/250 + guinea pig anti-parvalbumin 1/2000 or mouse anti-GAD67 1/1000 revealed by goat anti-rabbit-Alexa647 1/500 and goat anti-guinea pig-Alexa488 1/500 or donkey anti-mouse-Alexa488 1/500. dSTORM imaging was performed on a LEICA DMI8 mounted on an anti-vibrational table (TMC, USA), using a Leica HCX PL APO 160x 1.43 NA oil immersion TIRF objective and fiber-coupled laser launch (Roper Scientific, Evry, France). Fluorescent signal was collected with a sensitive EMCCD camera (Evolve, Photometrics, Tucson, USA). Experiments are realized as described in Haas et al., 2018.

The spinning disc microscope described was used for imaging of SSF-MOR and HA-MOR internalization in live MSNs with a 100x 1.49 NA objective. Neurons were transfected with syp-mCh and HA-MOR or SSF-MOR using lipofectamine, incubated for 10 min with alexa488 conjugated anti-HA antibody (Invitrogen) or M1-Alexa488 and washed 3 times with HBS before live cell imaging at 37°C. Time lapse was performed at 0.1Hz (HA-MOR) or 0.05Hz (SSF-MOR) and DAMGO 10μM added on stage after 1 min of imaging. The same system was used to monitor internalization of alexa488 conjugated dermorphin in syp-mCh expressing neurons. After 30 min of incubation with 1μM of fluorescent ligand, cells were washed 3 times with HBS and imaged live.

Photoactivation

Photoactivation of MOR-PAGFP was performed in HBS at 37°C on an Andor Borealis CSW-W1 spinning disc confocal Nikon Ti Microscope with Andor 4-line laser launch and a temperature, humidity- and CO₂-controlled chamber (Okolab). Neurons were transfected with syp-mCh and MOR-PAGFP using lipofectamine and were labeled with M1-a647 for 10 min before 3 washes with HBS. Depending on the condition, DAMGO 10 μM was added to the imaging media 1 minute before the beginning of the acquisition. Axons were imaged using a 100x 1.40 NA Plan Apo VC objective (Nikon) and an Andor iXon Ultra DU888 EMCCD camera controlled by MicroManager software. After one image in the red and far red channels, MOR-PAGFP was photoactivated at 2-3 synapses or extrasynaptic regions using a Rapp Optoelectronic UGA-40 system with 405 laser (Vortran). PAGFP fluorescence was monitored by acquiring images every 500ms before and after photoactivation.

Oblique illumination

HiLo imaging was performed on a Nikon Ti-E TIRF microscope equipped with an Andor iXon DU897 EMCCD camera controlled by NIS-Elements 4.1 software. Solid-state lasers of 405, 488, 561 and 647nm (Keysight Technologies) were used as light sources and samples imaged with an Apo TIRF 100x 1.49NA objective except when indicated. Microscope was also equipped with a perfect focus system and an objective and stage heater set to 37°C.

For imaging of syp-mCh and MOR-GFP, MSNs transfected with lipofectamine were washed and imaged in HBS or incubated for 20 min with DAMGO 10μM in HBS before imaging in HBS.

Imaging of surface MOR was performed on MSNs transfected with syp-mCh and SEP-MOR using lipofectamine, or nucleofected with syp-mCh and SSF-MOR after 10 min of incubation with M1a488. Cells were washed 3 times with HBS before imaging in both channels.

For imaging of SSF-MOR relocalization using the accumulation index measurement, MSNs nucleofected with syp-mCh and either wild-type SSF-MOR or the S/T to A mutant were incubated for 10 min with M1a647 at 37°C 5% CO₂ in culture media, plus Cmpd101 30μM, Dyngo-4a 30μM or DMSO 0.06% (vehicle control concentration) for the corresponding conditions. Cells were washed 3 times with HBS and incubated for 20 min at 37°C 5% CO₂ in HBS, HBS plus DAMGO 10μM and Cmpd101 30μM, Dyngo-4a 30μM or DMSO 0.06% depending on the condition.

To study the effect of Cmpd101 on SEP-MOR endocytosis, SEP-MOR and syp-mCh transfected MSNs were preincubated with Cmpd101 30μM or DMSO 0.06% in culture media at 37°C 5% CO₂ for 10 min, and DAMGO 10μM was added depending on the condition for another 20 min in the incubator. Cells were washed 3 times with HBS before imaging in HBS+DMSO 0.06%, HBS+DAMGO 10μM+Cmpd101 30μM or HBS+DAMGO 10μM+DMSO 0.06%. A Plan Apo VC 60x 1.4NA objective was used for this set of experiments, one frame was taken in both channels, coverslips washed with 4ml of ammonium chloride solution on stage before acquisition of another frame in both channels.

Imaging of β -arrestin2-GFP distribution in live MSNs transfected with syp-mCh and SSF-MOR using lipofectamine was performed after incubation for 10 min with M1-a647 in culture media. Cells were washed 3 times with HBS and imaged at 0.2Hz and DAMGO 10 μ M added during the acquisition. Imaging of SSF-MOR accumulation at VPS29-GFP labeled endosomes in syp-mCh marked axons was performed in the same conditions, but the frequency of acquisition was 1 frame per minute. To generate kymographs and movies showing movement of VPS29-GFP and internalized MOR, the same procedure was applied but MSNs were imaged at 1Hz after incubation with DAMGO 10 μ M for 20 min in imaging media in the incubator.

For imaging SSF-MOR containing endosomes, MSNs nucleofected with SSF-MOR and syp-mCh were incubated for 10 min with M1-a488. Neurons were washed 3 times in HBS and incubated for 20 min in HBS with 10 μ M DAMGO at 37 $^{\circ}$ C 5% CO₂. Images were taken in both channels or time series performed at 1Hz.

To quantify the density of VPS29-GFP marked endosomes and synapses, MSNs were transfected with VPS29-GFP and syp-mCh using lipofectamine and images acquired in both channels. For the TTX conditions, neurons were incubated for one hour with TTX 1 μ M in culture media in the incubator before 3 wash and imaging in HBS+TTX 1 μ M. For the untreated and high potassium conditions, cells were washed in HBS and mounted on the microscope stage, with 1ml of media for the high potassium condition. 1ml of HBS solution containing 24mM NaCl and 98mM KCl was added to 1ml of HBS at the beginning of the acquisition for the high potassium condition in order to achieve a final concentration of 50mM KCl and 72mM NaCl. 0.2Hz time lapse image series were acquired and quantification of endosomes densities performed at 1,2 and 3 min after high potassium addition.

For imaging of insertion events, MSNs nucleofected with SEP-MOR and syp-mCh were incubated for 20 min with DAMGO 10 μ M in culture media in the incubator. Cells were washed 3 times with HBS and mounted on stage with HBS or HBS+10 μ M DAMGO. After imaging of one frame in the red channel, axons were imaged at 10Hz in the green channel for 5 min. The same protocol was used to quantify the frequency of insertion events in calcium free HBS supplemented with 10 μ M DAMGO, or a solution containing 50mM potassium (1ml regular HBS and 1ml of the solution containing 98mM KCl described previously added right before the acquisition). The same protocol was used to quantify the effect of Cmpd101 on MOR insertion events frequency, but neurons were preincubated for 10 min in culture media in the incubator with Cmpd101 30 μ M or DMSO 0.06% vehicle and DAMGO 10 μ M was added for 20 other min before imaging.

To localize SEP-MOR insertion events relative to VPS29-mCh marked endosomes in morphologically identified axons, lipofectamine transfected MSNs were incubated for 20 min with DAMGO 10 μ M in the culture media in the incubator, washed 3 times with HBS and imaged in HBS + DAMGO 10 μ M at 2Hz in both channels using triggered acquisition.

We used the same imaging system for implementation of the pulsed pH. Axons of cultured MSNs rarely contact the coverslip, excluding the possibility of TIRF imaging of axons. We used oblique illumination on neurons expressing syp-mCh and SEP-MOR as the axonal pH5.5 resistant fluorescent cellular background was minimal in the green channel and allowed for the unambiguous detection of endocytic events. After coverslips were washed with HBS, DAMGO 10 μ M was added to the imaging media depending on the condition. Cells were mounted on the heated stage of the TIRF microscope for imaging in oblique illumination. For the solution exchange, a theta pipet with a tip of about 100 μ m was placed close to the recorded area. It contained HBS pH7.4 + 500 μ M amiloride \pm 10 μ M DAMGO in one channel, and in the other channel a pH5.5 solution supplemented with amiloride and \pm DAMGO as well. pH5.5 solution was similar to HBS except that 10mM HEPES was replaced with 10mM MES and pH adjusted to pH5.5. Solution flow was alternated in synchronicity with 0.5Hz image acquisition every 2 s with electrovalves (The Lee company) controlled by a custom-built device.

For uPAINT imaging, axons of neurons transfected with SEP-MOR and syp-mCh were imaged in oblique illumination for one frame both in the green and red channel. A low concentration of anti-GFP nanobody conjugated to ATTO-647N was added to the media before acquisition. When performing the uPAINT experiment in the presence of agonist, DAMGO 10 μ M was added together with the ATTO647-Nb. We performed 256*256 pixels 45Hz acquisition in the far-red channel for a total of 20 000 frames. Each frame exhibited diffraction limited bright spots corresponding to individual molecules. PALM imaging of MOR-mEos2 was performed at 45Hz on a 256*256 pixels area of the camera on axons of MSNs identified by VGAT-SEP. mEos2 single molecules were photoconverted with 405nm and simultaneously imaged with 561nm illumination. 405nm light intensity was adjusted to achieve an appropriate density of single molecules, total acquisition was 20 000 frames. For both single-molecule approaches, specificity of labeling was confirmed by the negligible number of detections in areas of the images where no transfected neuron was present.

Statistics

Quantification of data are presented as mean \pm standard error of the mean (SEM) based on at least 2 independent neuronal cultures. The precise number of independent experiments and sample size is indicated in the figure legends. Statistical analysis was performed with Excel (Microsoft office, 2016) using unpaired Student's t test except when indicated otherwise. Statistical significance of cumulative frequencies accumulation index curves difference was estimated using two-samples Kolmogorov-Smirnov test performed with MATLAB.

Quantitative image analysis

Except when specified, image analysis was performed on unprocessed TIFF images using custom scripts written in MATLAB.

To quantify the average Alexa647 fluorescence on maximal projection from spinning disc images of HEK293 cells, a polygon was drawn around the contour delineated by the TRF-SEP fluorescence and the average fluorescence in the far-red channel was

background subtracted. To quantify the expression level of MOR in the different neuronal systems, background subtracted average fluorescence was calculated along a 3-pixels wide linescan in the far-red channel.

To quantify the amount of intracellular SEP-MOR before and after treatment with DAMGO, 5 pixels wide lines were drawn on axons identified with syp-mCh on the frames following the ammonium chloride perfusion. Quantification of Δ was done by subtraction of the average linescan fluorescence value of the frame in ammonium chloride minus the preceding frame in HBS. Normalized $\Delta F/F$ was calculated by dividing the Δ value by the background corrected fluorescence value in the presence of ammonium chloride solution. Paired Student's t test were used to evaluate the statistical significance of this result. Same analysis was performed with 3-pixel lines to quantify the fluorescence difference in DMSO, DMSO+DAMGO and Cmpd101+DAMGO but using unpaired Student's t test.

To determine a linear correlation coefficient between syp-mCh and MOR-GFP, a 1-pixel wide line was drawn on individual synapses, the fluorescence profile obtained in both channels for each synapse was normalized with the maximal value set to 1 and the minimal value set to 0. Linescans in both channels were aligned to the maximal value in the mCherry channel. A similar approach was used to quantify M1-a647 labeled surface MOR enrichment at VPS29-GFP labeled endosomes before and after DAMGO addition, with the average fluorescence of 3 pixels wide linescan and the GFP channel used for reference for the alignment. The linear correlation coefficient was calculated for every VPS29-GFP marked endosome as the value of the normalized 647 channel at the maximal GFP value. Paired Student's t test were used to evaluate the statistical significance of the linear correlation coefficient. To quantify the difference in distribution of MOR-GFP in the absence or presence of agonist, a different normalization approach was used to highlight differences in amplitude. Fluorescence measurements from a 1-pixel wide linescan were background subtracted and normalized as follow: $F = (FL - F_{min}) / (F_{max} - F_{min})$ where F_{max} is the maximal value along the linescan, F_{min} the minimal value along the linescan, FL the value at the corresponding position on the linescan. Normalized linescans were aligned to their respective maximal value for both channels.

To quantify the synaptic enrichment of SEP-MOR or M1-a488 labeled SSF-MOR at synapses labeled with syp-mCh, 1-pixel wide lines were drawn on individual synapses and immediately neighboring axonal shaft. After background subtraction, average fluorescence in the synaptic area was normalized by the average fluorescence outside of the synapse. Paired Student's t test were used to evaluate the statistical significance of this result.

To achieve unbiased quantification of opioid receptor redistribution in axons, while making the analysis compatible with endogenous receptor localization, we defined an 'accumulation index'. This metric takes advantage of the fact that receptors present in the axon surface are diffusely distributed along the axon length but, when internalized, receptors accumulate in punctae. The accumulation index was calculated on HiLo images (MSNs) or maximal projection from spinning disc Zstacks (habenula neurons) by quantifying the background subtracted average fluorescence of 3 pixels wide lines drawn on axonal segments for each position on the linescan. For each segment, the index was the difference of the average of the 5% brightest values minus the average fluorescence of the 50% dimmest values, normalized by the average value obtained for the whole segment. Values calculated from line scan analysis of individual axon segments are plotted, over a large number of segments analyzed, as a cumulative frequency distribution. Punctate redistribution of receptors, correlating with internalization, is indicated by a right shift in this cumulative frequency curve.

Tracking of endosomes was performed manually on 1Hz movies of internalized SSF-MOR. Tracking lasted for as long as the endosome was unambiguously identified, and stopped when endosome was moving out of focus or crossing another endosome. Instant speed was calculated as the distance traveled between two frames, sorted for intra-synaptic movement or extrasynaptic movement. Movement into or out of synapses were not considered for this analysis. Mean square displacement for either synaptic or extrasynaptic trajectories was calculated using the same formula as for single particle tracking (see below).

For the quantification of the SSF-MOR enrichment at VPS29 sites, VPS29-GFP image series were divided into subregions containing axons labeled with syp-mCh. These movies were manually thresholded to encompass VPS29-GFP endosomes and generate a mask of the structures through the whole time series. After filtering to exclude objects smaller than 5 pixels, remaining objects were then smoothed with a dilatation of 1 pixel before an erosion of 1 pixel. The generated mask was applied to the SSF-MOR channel in order to quantify the fluorescence at VPS29-GFP objects and the average fluorescence in the mask was background subtracted and normalized to the average fluorescence of the 5 frames preceding DAMGO addition.

For quantification of SEP-MOR exocytosis, image series were reviewed and exocytic events manually registered. The insertion site was scored relative to the synapse and fluorescence quantified in a 2.2 pixels radius circle centered on the event. Fluorescence curves were normalized as follows: the average fluorescence of the 10 frames before exocytosis was considered background and subtracted to the signal. The fluorescence curve was then normalized with the maximal fluorescence value of the frames 0-5 after insertion set to 100%. The fluorescence half time was scored as the first time point where the normalized fluorescence was less than 50%. Frequency of exocytosis was defined as the ratio of the number of detected events by the length of the acquisition, and normalized by the number of synapses in the imaging field for accurate comparison between acquisition. Paired Student's t test were used to evaluate the statistical significance of the frequency of exocytosis inside and outside of synapses.

Quantification of the density of synapses and VPS29-GFP marked endosome were made by manually counting the corresponding structures in both channels along measured axonal segments.

For endocytosis of SEP-MOR, pH5.5 image series were reconstructed after separation of the pH7.4 and pH5.5 frames. Sudden appearance of a pH5.5 resistant fluorescent signal were manually registered and reviewed together with the pH7.4 frames and

the syp-mCh images to classify them as endocytic (signal stable at pH7.4) or kiss and run (coincident burst of fluorescence at pH7.4) events, and their position scored relative to synapses. Fluorescence was then quantified in a 2.2 pixels radius circle centered on the event. Frequencies of endocytosis were normalized as for frequency of exocytosis. Paired Student's t test were used to evaluate the statistical significance of the frequency of endocytosis inside and outside of synapses.

Quantification of the presynaptic response signal upon electrical field stimulation was performed by averaging the fluorescence of in-focus VGAT-SEP expressing synapses. Synapses were manually picked on a differential image before/after addition of ammonium chloride. Fluorescence was quantified in a 2.2 pixels radius circle centered on each synapse, and normalized by the fluorescence in the presence of ammonium chloride. The normalized fluorescence signal of each synapses for a given stimulation for the 10 frames preceding the stimulation was used to define the baseline and set to 0. To plot the fluorescence increase upon electrical field stimulation, normalized fluorescence curves were averaged across cells and stimulations. To quantify the amplitude of fluorescence increase upon electrical field stimulation, the maximal normalized fluorescence value of the first 5 time points after stimulation was scored as the amplitude and averaged across synapses for each cell. For the quantification of endogenous MOR inhibition of synaptic vesicle exocytosis in habenula neurons, only synapses with an average baseline (first 5 stimulations) response ≥ 0.02 A.U. were used for the analysis.

dSTORM experiments are realized as described in Haas et al., 2018 and super-resolution images with a pixel size of 25 nm were reconstructed using WaveTracer software (Kechkar et al., 2013) operating as a plugin of MetaMorph software. To estimate the density of endogenous MOR in axons and synapses, the intensity of secondary antibodies bound to the coverslip were used to estimate the dSTORM detection signal corresponding to individual molecule. This was used to calibrate the signal of single MOR receptors in axons. A typical uPAINT or PALM experiment acquired with the microscope setup and protocol described above produced a set of 20,000 images that were analyzed to extract molecule localization and dynamics. Single molecule fluorescent spots were localized and tracked over time using a combination of wavelet-based segmentation and simulated annealing tracking algorithms using a software package a custom written plug-in running within the MetaMorph software environment as previously described (Nair et al., 2013; Rossier et al., 2012). The mean square displacement (MSD) and diffusion coefficient (D) were calculated for every trajectory as follow. For every trajectory of N data points (coordinates $x(t)$, $y(t)$ at times $t = 0$ to $(N-1)*\Delta t$ with $\Delta t = 22\text{ms}$), the MSD for time intervals $\tau = n*\Delta t$ is calculated using the formula:

$$\sum_{i=1}^{N-n} \frac{[x((i+n)*\Delta t) - x(i*\Delta t)]^2 + [y((i+n)*\Delta t) - y(i*\Delta t)]^2}{N-n}$$

To define the diffusion profile across the different conditions, we included only trajectories longer than 6 points. This allowed for the exclusion of non-specific detections and reconstructed trajectories were overlapping with the area of transfected axons. The diffusion coefficients D for each trajectory were extracted by linear fitting on the first 4 time points of the MSD curves using the formulae $\text{MSD}(\tau) = \langle r^2 \rangle (\tau) + \alpha = 4D\tau + \alpha$, with α the ordinate at the origin of the linear fit due to the precision accuracy in the localization process. The bin at $10^{-5} \mu\text{m}^2.\text{s}^{-1}$ represents trajectories for which calculation of D was $\leq 10^{-5} \mu\text{m}^2.\text{s}^{-1}$. Super-resolution images were generated to display localization intensities, reconstructed individual trajectories, localization density of mobile molecules ($D \geq 10^{-2} \mu\text{m}^2.\text{s}^{-1}$), immobile molecules ($D \leq 10^{-2} \mu\text{m}^2.\text{s}^{-1}$), or diffusion coefficients maps. Diffusion coefficients maps were computed by calculating averaging in each pixel the diffusion coefficients from all the trajectories detected in the corresponding pixel.

Quantification of the fluorescence decay of PAGFP-MOR was calculated by generating a mask of the photoactivation area of the axon in an area of the time series that encompass the photoactivated area. The mask was generated by thresholding the result image of the difference of the first frame after photoactivation minus the frame before activation. Fluorescence was quantified in the corresponding mask through the time series and normalized so the maximal fluorescence value after photoactivation was set to 1 and the average fluorescence before photoactivation set to 0. Because the diameter of axons (and consequently of the photoactivated area) was variable, this approach was limited to the study of an immobile fraction.

Modeling

Computer modeling were performed using the MCell/CellBlender simulation environment. The realistic model of glutamatergic synaptic environment was constructed from 3D-EM of hippocampal area CA1 neuropil as described in (Bartol et al., 2015a, 2015b; Kinney et al., 2013). The 3D-EM reconstruction is highly accurate and detailed and contains all plasma membrane bounded components including dendrites, axons, astrocytic glia and the extracellular space itself, in a $6 \times 6 \times 5 \mu\text{m}^3$ volume of hippocampal area CA1 stratum radiatum from adult rat. For these models, a segment of axon containing two presynaptic terminals was used. The axonal plasma membrane was associated with two surface properties: the axon shaft and the active zone defined as the area facing the postsynaptic densities. Simulations were performed at the μs timescale.

The various interactions are implemented following the scheme presented Figures S5G and S5H with binding constant for dermorphin obtained from the literature (Birdsong et al., 2013). Homogeneous ligand concentration was simulated by associating a uniform binding probability to each receptor reflecting the k-on for dermorphin ($k\text{-on} = 494200 \text{ M}^{-1}.\text{s}^{-1}$) and a concentration of dermorphin of 100 nM. Except when specified, we used values of $K = 5 \text{ s}^{-1}$, an average diffusion coefficient of $0.1 \mu\text{m}^2.\text{s}^{-1}$ and a density of 50 receptors. μm^{-2} . K-off for dermorphin was 0.05 s^{-1} , and the different affinity values were simulated by adjusting the k-off only. The inter-

action constants varied in function of the simulation as detailed in the figure legends, and 10 simulation trials were averaged for each condition.

DATA AND CODE AVAILABILITY

The custom written scripts supporting this study have not been deposited in a public repository because they require extensive user experience to navigate, but are available from the corresponding author on request.